OPEN ACCESS

University of BRISTOL

Kamliya Jawahar, H., Alihan Showkat Ali, S., Azarpeyvand, M., & Ilário da Silva, C. R. (2020). Aerodynamic and aeroacoustic performance of high-lift airfoil fitted with slat cove fillers. *Journal of Sound and Vibration*, *479*, [115347]. https://doi.org/10.1016/j.jsv.2020.115347

Peer reviewed version

License (if available):
CC BY-NC-ND

Link to published version (if available):
10.1016/j.jsv.2020.115347

Link to publication record in Explore Bristol Research
PDF-document

This is the author accepted manuscript (AAM). The final published version (version of record) is available online via Elsevier at https://www.sciencedirect.com/science/article/abs/pii/S0022460X20301784. Please refer to any applicable terms of use of the publisher.

University of Bristol - Explore Bristol Research
General rights

This document is made available in accordance with publisher policies. Please cite only the published version using the reference above. Full terms of use are available:
http://www.bristol.ac.uk/red/research-policy/pure/user-guides/ebr-terms/

Aerodynamic and Aeroacoustic Performance of High-lift Airfoil Fitted with Slat Cove Fillers

Hasan Kamliya Jawahar[a,*], Syamir Alihan Showkat Ali[a,b,**], Mahdi Azarpeyvand[a,], Carlos R. Ilário da Silva[c,]

[a] *Department of Mechanical Engineering, University of Bristol, Bristol BS8 1TR, UK*
[b] *School of Manufacturing Engineering, Universiti Malaysia Perlis, 02600, Perlis, Malaysia*
[c] *Embraer, São José dos Campos, 12227-901, Brazil*

Abstract

Experimental measurements were carried out to assess the aerodynamic and aeroacoustic performance of an MDA 30P30N airfoil fitted with two different types of slat cove fillers. The aerodynamic results are presented for lift and drag measurements and mean surface pressure measurements, while the aeroacoustic results are presented for the near-field surface pressure fluctuations and far-field noise measurement. The flow measurement results show that there is no significant difference in the aerodynamic lift and drag between the tested cases, however, the slat cove filler configurations exhibit a much better lift-to-drag performance. The pressure coefficient results show that the use of slat cove fillers leads to a slight decrease in the suction peak over the main-element of the airfoil. In order to better understand the flow-field and the noise generation mechanism of the airfoil with slat cove fillers, simultaneous near-field and far-field noise measurements were carried out. The result shows that the use of the slat cove filler can generally lead to a significant reduction of the broadband noise and eliminate the characteristic tonal noise generated by the slat. The directivity pattern and the overall sound pressure level of the radiated noise have shown that a significant noise reduction can be achieved with the applications of the slat cove fillers. The multiple tonal phenomena generated by the slat were also analysed using the continuous wavelet transform method and higher order spectral analysis methods.

Keywords: 30P30N, High-lift airfoil, Slat noise, Slat cove filler, Aeroacoustics.

[*] Research Associate, Department of Mechanical Engineering
[**] Lecture, Department of Mechanical Engineering
Corresponding Author, Professor in Aeroacoustics, Department of Mechanical Engineering
Technology Development Engineer, Embraer
Email addresses: hasan.kj@bristol.ac.uk (Hasan Kamliya Jawahar), syamir@unimap.edu.my (Syamir Alihan Showkat Ali), m.azarpeyvand@bristol.ac.uk (Mahdi Azarpeyvand), carlos.ilario@embraer.com.br (Carlos R. Ilário da Silva)

1. Introduction

THE impact of aircraft noise on the communities near the airports has been an issue since the entry of turbofan and turbojet engines into civil aviation in the 1960s and 1970s. The widespread global expansion of air travel has made the environmental impact of aircraft noise much more prominent in recent times. This has forced the International Civil Aviation Organisation (ICAO) to set technical standards for civil air transport aircraft, which has been adopted by over 180 countries. With such upcoming regulations to reduce noise impact on communities near the airports, further understanding of aircraft noise has to be achieved. The introduction of high bypass-ratio turbofan engines into civil aircraft have drastically reduced engine jet noise over the last several decades, making the airframe noise one of the main contributors to the overall aircraft noise, especially during the landing phase. One of the main sources of the airframe noise is due to the high-lift devices, namely the slat and flap. In order to reduce these prominent noise sources several passive and active flow control methods have been investigated in the past, such as, morphing structures [1–5], porous materials [6–8], surface treatments [9] and serrations [10, 11].

Studies on conventional slat and wing configurations have shown that the radiated noise comprises both broadband and tonal noise components. Choudhari and Khorrami [12] showed that the overall slat noise is generated from the unsteady flow within the slat cove region originating from the vortex shedding at the slat cusp and the slat trailing edge. Terracol *et al.* [22] showed that the strong tonal peak in the mid-frequency range ($St_s = 1 - 5$) is generated due to the flow acoustic feedback of slat cove shear layer instabilities, which has also been observed in other studies [12–22, 24–31]. The results are also indicative that the tonal peaks are associated with the cavity feedback mechanism, known as the Rossiter modes [56, 57]. A possible quadratic interaction between the tonal peaks has also been observed [23–27]. Apart from these discrete tones, a spectral hump at low-frequency range ($St_s < 1$) were identified in recent studies [22, 26, 28–31]. Pascioni *et al.* [26] suggested that the low-frequency broadband hump at $St_s > 1$ is related to the slat cove bulk-oscillation, which is associated with the flapping of the slat cusp shear layer. At high frequencies ($St_s \approx 30$) tonal peaks are observed, Khorrami *et al.* [15] showed that these high-frequency tonal peaks are related to the flow velocity and the slat trailing edge thickness, this was also verified later by Olson *et al.* [14]. Despite the progress in understanding the slat noise, it still remains the main contributor of airframe noise. Therefore, there is still a demand for further fundamental studies into the slat noise generation mechanism and ways to suppress them.

Several experimental and computational studies were conducted in the past decade to investigate and reduce the broadband noise arising from within the slat cove region by casing the recirculation region [32–42]. The results showed that the use of slat cove filler (SCF) leads to a marginal reduction of the broadband noise and elimination of the tonal peaks at all the instances. However, the aerodynamic performance of the slat cove filler configuration is yet to be thoroughly documented. The approach of filling the slat cove region to reduce noise is based on eliminating the strong shear layer created after the slat cusp and avoiding the development of complicated flow structure within the slat cove region by using a smoothly contoured profile. In order to eliminate the unsteady recirculation region within the slat cove, Horne *et al.* [32] from NASA tested a solid SCF on a Boeing 777-200 semi-span model in the NASA Ames 40 by 80 foot Wind Tunnel. The SCF profiles were derived from

a CFD analysis in order to maintain attached flow on the slat pressure surface. The experiments used a microphone phased array and the results showed that the SCF was effective in reducing the broadband slat noise up to 4-5 dB. However, no aerodynamic measurements were presented in this study. Streett *et al.* [33] further investigated the noise and basic aerodynamic performance of the SCF setup using a trapezoidal wing swept model fitted. The results showed noise reduction to be sensitive to the angle of attack and SCF modification. The SCF modification showed a reduction of up to 3-5 dB over a wide spectrum. The aerodynamic performance appeared marginally better than the Baseline at the angle of attack below $\alpha = 20^{\circ}$ and the stall occurred 2-degrees earlier compared to the Baseline. The specific reason for the loss in aerodynamic performance was not pointed out due to the lack of aerodynamic data, such as detailed surface pressure and wake shear layer measurements.

Imamura *et al.* [36] and Ura *et al.* [37] from JAXA further validated that noise reduction can be achieved by the use of SCF. However, the SCF was found to affect the aerodynamic lift characteristics of the 30P30N airfoil. The SCF profiles were designed based on the flow field streamlines at the angles of attack $\alpha = 0^{\circ}$ and 8°. Even though the results showed a reduction of up to 5 dB for both the cases, the aerodynamic performances were the same as that of the Baseline only for the 8-degree SCF profile. However, in the case of 30P30N airfoil fitted with the 0-degree SCF profile, the airfoil stalled prematurely. In an optimization study, Tao and Sun [41] performed several simulations using 44 configurations of the SCF profile designs aimed to produce maximum lift coefficient for fixed design point with an angle of attack of $\alpha = 22^{\circ}$ and $Re_c = 9 \times 10^6$. The final optimized SCF profile showed a reduction in noise while maintaining the aerodynamic performance. In a very recent study, Zhang *et al.* [42] showed that the use of passive treatments on the slat, such as slat extensions, gap fillers and cove fillers, exhibit minimal detrimental effect on the mean pressure distribution of the high-lift device. They also showed that the proposed passive devices suppress the slat cavity tonal peaks, as well as shifting them to higher frequencies. Amongst the tested passive devices, slat cove fillers were found to demonstrate the most effective performance.

This study presents a detailed aerodynamic and aeroacoustic analysis of a high-lift 30P30N airfoil compared with two slat cove filler cases. It is important to note that the 30P30N airfoil used in this study is of a different size with a smaller chord and finite span compared to the BANC benchmark model [23] and, as a result, the aerodynamic and noise data will not be easily comparable to those of BANC [27, 32]. The main purpose of this study is to provide a parametric study for the use of slat cove fillers using the existing high-lift device, rather than providing a comparison against the BANC dataset [27, 32]. Despite the above-mentioned size difference, the data collected using the current 30P30N in our study are analyzed and compared against the existing and comparable test cases presented in the literature [28], which will be presented in Section 3. The paper is organized as follows: Section 2 describes the wind tunnel setup, the SCF setup and the high-lift airfoil instrumentation. Section 3 reports the aerodynamic results, which presents the aerodynamic forces such as lift and drag measurements and coefficient of pressure distribution around the airfoil. Section 4 reports the detailed aeroacoustic results, which presents the far-field spectral levels, near-field spectral levels, spanwise coherence, correlation length scales, continuous wavelet transform of the near-field measurements, higher order spectral analysis of the near-field measurement and persistence spectrum of the near-field measurements. Finally, Section 5 presents an overall summary of the work and conclusions.

2. Experimental setup

2.1. Airfoil setup

An MDA 30P30N three-element high-lift airfoil with a retracted chord length of $c = 0.35$ m and a span length of $l = 0.53$ m was manufactured using a computer-aided numerically controlled machine. The geometrical parameters of the high-lift airfoil are shown in Fig. 1 and Table 1. In order to maintain two-dimensionality within the slat cove and main-element cove regions, no brackets were used in the spanwise direction. All the three-elements were held together by steel clamps from the sides of the airfoil. The Cartesian coordinate system (x, y, z) starts from the leading edge point of the retracted 30P30N airfoil, as shown in Table 2. The airfoil was equipped with 103 static pressure measurement taps placed along the mid-span of the airfoil. In order to ensure turbulent flow within the slat cove region a sandpaper trip (80 grit) with a thickness of $h = 0.6$ mm and a width of $w = 3$ mm at location $x/c = -0.055$ on the pressure side of the slat surface just upstream of the slat cusp [18]. Several tests were conducted with and without the boundary layer trips, and the results revealed that the aerodynamic and aeroacoustic measurements were independent of the use of trip for the tested configuration and flow conditions.

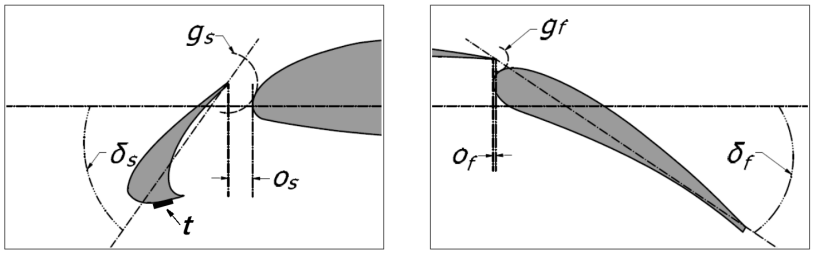

(a) (b)

Figure 1: The MDA 30P30N three-element high-lift airfoil geometric parameters.

Slat chord	c_s	$0.15c$
Main-element chord	c_{me}	$0.83c$
Flap chord	c_f	$0.3c$
Slat deflection angle	δ_s	$30°$
Flap deflection angle	δ_f	$30°$
Slat gap	g_s	2.95%
Flap gap	g_f	1.27%
Slat overhang	o_s	-2.5%
Flap overhang	o_f	0.25%
Tripping device	t	0.6×3 mm

Table 1: Geometrical parameters of the 30P30N high-lift airfoil in percentage of stowed airfoil chord, $c = 0.35$ m.

2.2. Wind tunnel and measurement setup

The aerodynamic measurements were carried out in the large low-speed closed-circuit wind tunnel at the University of Bristol. The wind tunnel has an octagonal working area of 2.1 m × 1.5 m × 2 m and a contraction ratio of 3:1. The wind-tunnel is capable of a maximum velocity of 60 m/s with typical turbulence intensity levels as low as 0.25%. The aeroacoustic measurements were carried out at the aeroacoustic wind tunnel facility at the University of Bristol. This is a closed circuit open-jet anechoic wind tunnel with a nozzle exit of 0.775 m × 0.5 m and a contraction ratio of 8.4:1 providing turbulence levels as low as 0.25% [43, 44]. The flow turbulence intensity (TI) is calculated using $U^{'}_{rms}/U_{mean}$, where $U^{'}_{rms}$ is the root-mean-square of the velocity fluctuations and U_{mean} is the average velocity. The velocity fluctuations have been high-pass filtered at $f = U_{\infty}/2L_{TS}$, where L_{TS} is the largest test section dimension, in order to remove the effect of large-scale facility unsteadiness from the turbulence intensity measurement.

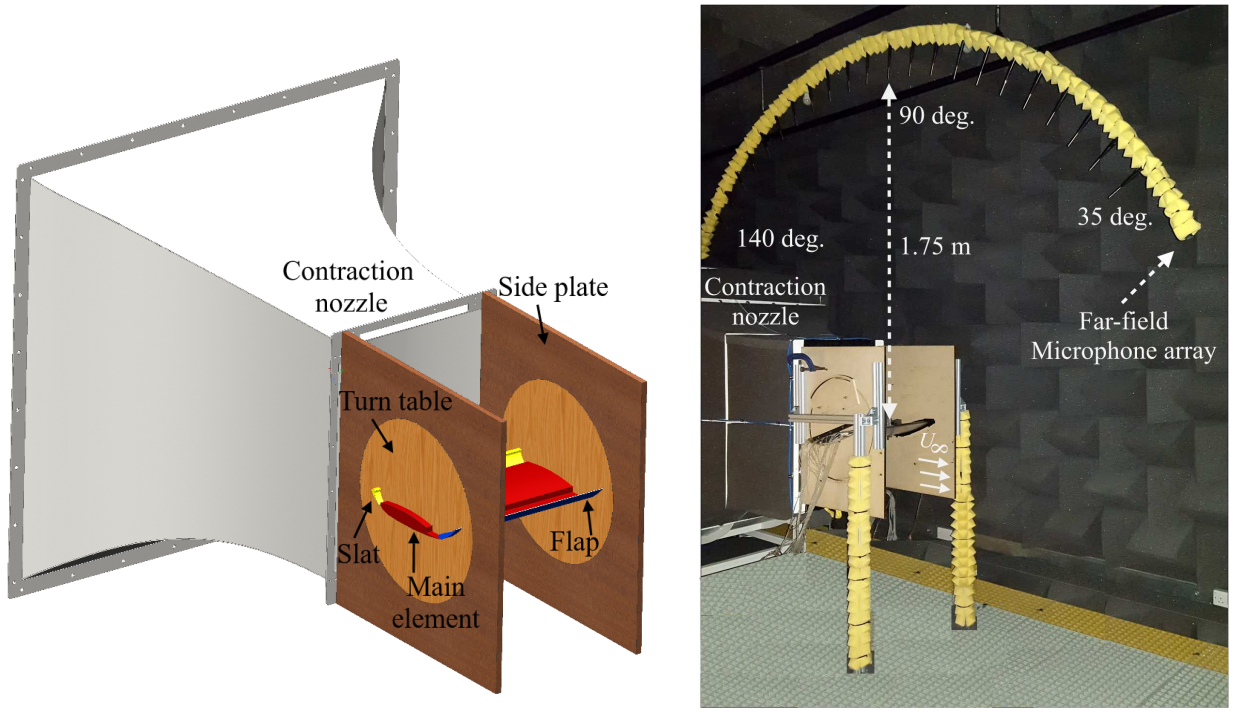

(a) (b)

Figure 2: (a) A schematic of the 30P30N airfoil mounted on the wind tunnel and (b) Test model mounted in the aeroacoustic wind tunnel at the Univertsity of Bristol.

The lift and drag measurements were carried out using an AMTI OR6-7-2000 force platform from Advanced Mechanical Technology Inc. The airfoil was secured to the force platform using two teardrop shaped metal side-arms to minimise the drag forces on the support arms. The force platform records the force-induced voltage, which is measured through the AMTI MSA-6 strain gauge amplifiers and processed using the in-built LabView V18 system design software. The data were collected through a 16-bit A/D card for a period of 16 seconds at a sampling frequency of 2000 Hz, which deemed sufficient enough based on an uncertainty

analysis of the collected data. The uncertainty analysis was found to be $\approx 4.5\%$ at a 95% confidence level for all the tested angles of attack.

The static pressure measurements around the airfoil were carried out using MicroDaq pressure scanners manufactured by Chell Instruments. Two scanners equipped with 32 channels were used to measure the surface pressure. The scanners have a full-scale measuring capacity of 1 Psi with a system accuracy of $\pm 0.05\%$. The data were collected at a frequency of 500 Hz for 60 seconds. The uncertainty analysis at all the angles of attack for the collected data was found to be $\approx 2\% - 9\%$ at a 95% confidence level depending upon the pressure tap location.

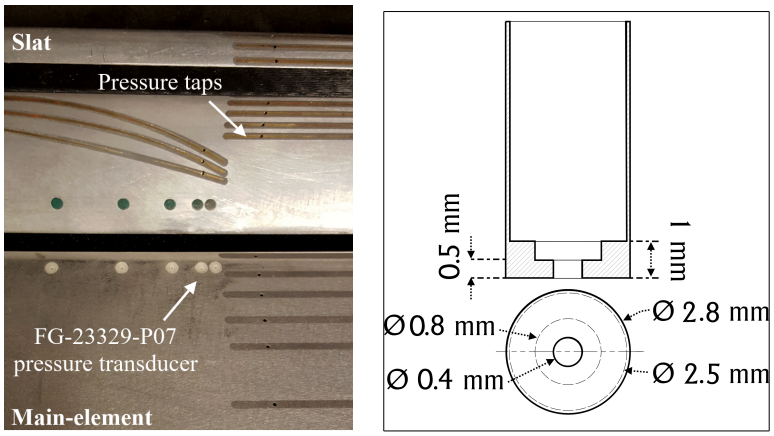

(a) (b)

Figure 3: (a) Surface mounted FG-23329-P07 pressure transducer with surface fairing and pressure taps on the main-element and slat of the 30P30N high-lift airfoil and (b) A schematic of the surface fairing for the pressure transducer.

To better understand the flow characteristics around the MDA 30P30N airfoil, unsteady surface pressure measurements were carried out using several FG-23329-P07 transducers (see Table 2) [47–50]. The transducer has a diameter of 2.5 mm and a height of 2.5 mm with a sensing area diameter of 0.8 mm. In order to reduce the measurement errors that arise due to the spatial integration of the signal, a surface fairing with a reduced sensing area of 0.4 mm was used (see Fig. 3). The transducers were installed on the main-element of the wing. The unsteady surface pressure measurements were carried out using a National Instrument PXle-4499 for 16 seconds at a sampling frequency of $f = 2^{16}$ Hz. The surface pressure data obtained give an absolute uncertainty of $\pm 0.05\%$ dB with 95% of confidence level.

The experimental setup of the high-lift airfoil for the aeroacoustic measurements is shown in Fig. 2. The far-field noise measurements were carried out using an array of 22 G.R.A.S. 40PL piezoelectric free-field microphones distributed over a circular arc at a radius of 1.75 m from the trailing edge of the slat. The microphone array covered a range of polar angles between 35° to 140°, with a regular interval of 5°. The G.R.A.S. 40PL microphone has a flat frequency response at frequencies from 10 Hz to 10 kHz, with a dynamic range of 142 dB. The far-field noise data were captured for $t = 16$ s at a sampling frequency of $f = 2^{16}$ Hz. The acoustic data were recorded for a wide range of flow velocities of up to 40 m/s.

Schematic	No.	x (mm)	z (mm)
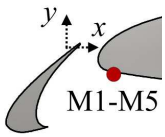	M1	22.414	277
	M2	22.414	280.6
	M3	22.414	288.4
	M4	22.414	301.4
	M5	22.414	319.6

Table 2: Pressure transducer locations on the MDA 30P30N airfoil.

In order to address the effect of the airfoil and side-plate junction noise and to evaluate the ability of an individual microphone to capture the slat noise, a thorough acoustic beamforming study using an array of 63 free-field microphones was carried out. The results showed that the wing and side-plate junction noise was not a major contributor to the far-field noise for the frequencies considered in this study. The results showed that the junction noise does not contribute significantly before 3600 Hz (St_s ≈6.2) and instead reveals that the noise originates from the slat area, distributed over the span of the wing. The point spectrum results from the far-field individual microphone were also observed to follow the same trend as the beamforming results. The results also accurately captured the characteristic tonal peaks and broadband hump that arises from the slat. Pascioni *et al.* [27] had also analyzed the accuracy of the far-field acoustic spectra based on individual microphones relative to beamforming results and Curle's acoustic analogy. The results from their study had also shown that the individual far-field microphones were sufficient enough to capture the dominant characteristic features of the slat noise.

The power spectrum results were obtained using the power spectral density (PSD) of the pressure signals with Hanning window and the acquired data were averaged for 200 times to yield a frequency resolution of $\Delta f = 6.25$ Hz. The sound pressure level (SPL) spectrum can then be calculated from $SPL = 20 \cdot log10(p_{rms}/p_{ref})$, where p_{rms} is the root-mean-square of the acoustic pressure and $p_{ref} = 20$ μPa is the reference pressure. The SPL of the acoustic pressure signal for the far-field measurement is corrected to a reference distance of 1 m. The overall sound pressure level was resolved for a frequency range from $f = 100$ Hz to 32 kHz.

2.2.1. Slat cove-filler design

As part of the noise reduction study of the MDA 30P30N airfoil, a slat cove-filler (SCF) was designed using a similar strategy introduced by Imamura *et al.* [36, 37] for experimentation purposes. Initially, a preliminary Reynolds-averaged NavierStokes (RANS) steady-state simulation for the Baseline case was performed at the angle of attack 8°. The slat shear layer trajectory profile with high turbulent kinetic energy (TKE) extracted from the results were used to define the shape of the SCF profile. Another configuration with a Half slat cove filler (H-SCF) was also considered, which exhibits good aerodynamic and noise reduction properties, as shown computationally by Tao [41]. Both the slat cove-fillers and the flap cove-fillers (FCF) were manufactured using 3D printing technology and was manufactured in four different sections that could be slid along the span of the slat and main-element cove. The solid 3D printed SCF is fitted with 6 pressure taps and the solid FCF is fitted with 3 pressure taps along the mid-span of the wing for surface pressure measurements. A schematic

of the different MDA 30P30N airfoil configurations used in the present study are shown in Fig. 4.

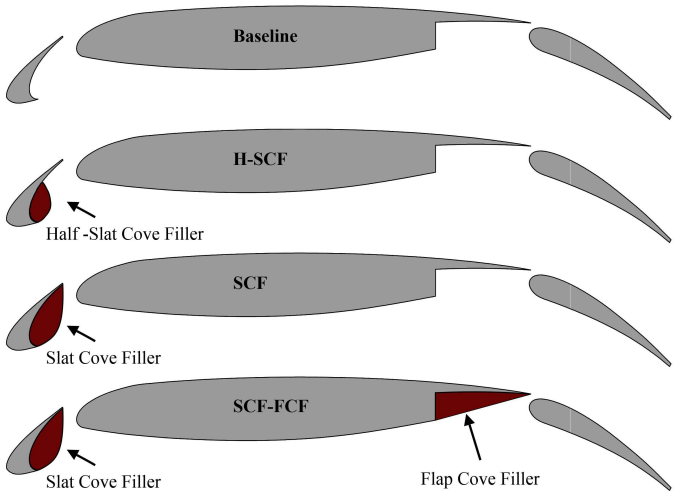

Figure 4: The MDA 30P30N Baseline airfoil fitted with half-slat cove filler (H-SCF), slat cove filler (SCF) and flap cove filler (FCF).

3. Aerodynamic results

To gain a better understanding of the aerodynamic performance of the MDA 30P30N airfoil, lift and drag measurements, and surface pressure distribution measurements were carried out. The high-lift airfoil was equipped with 103 pressure taps to accurately capture the surface pressure distribution over all the three components of the 30P30N high-lift device. It is noteworthy that the aerodynamic tests were carried out in the large low-speed closed-circuit wind tunnel and the results in this section are presented in terms of the geometric angle of attack. The high-lift airfoil was tested for a range of angles of attack from $\alpha = 0^\circ$ to 18° at the free-stream velocities of $U_\infty = 20$, 30, 40 and 47 m/s. The tested configurations were the Baseline, Half-slat cove-filler (H-SCF), Slat cove-filler (SCF) and Slat cove-filler along with Flap cove-filler (SCF-FCF), as shown in Fig. 4.

3.1. Test conditions

Previous experimental studies [28, 45] have shown that the flow field around the high-lift airfoils could be influenced by the size and type of the wind tunnel they are tested in. It is a common practice to compare the experimental results against numerical simulations with ideal free flight boundary conditions to determine the effects of the wind tunnel on the flow field. Li *et al.* [28] have shown that the pressure coefficient and flow field results for a 30P30N high-lift airfoil tested in a closed hard-wall wind tunnel were similar to that of the ideal free flight conditions, whereas the tests in an open test section wind tunnel resulted in the pressure coefficient and flow field different from the ideal free flight conditions (see Fig. 5(a)). Li *et al.* [28] concluded that the differences in the pressure coefficient and flow field are due to the high camber of the high-lift airfoil and interference from the wind tunnel sidewalls. The pressure coefficient results of the tests carried out at the large low-speed closed-circuit wind

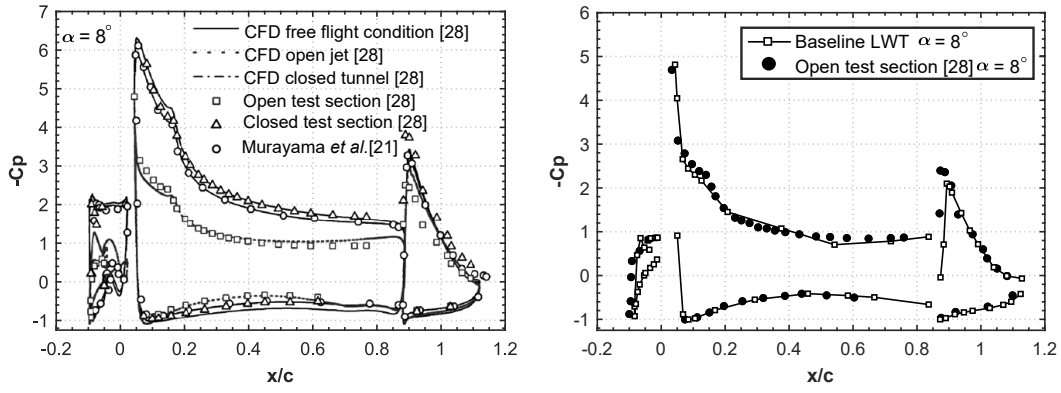

(a) (b)

Figure 5: (a) Pressure coefficient distribution over a 30P30N high-lift airfoil in different test conditions extracted from Li *et al.* [28] (b) Pressure coefficient distribution of the 30P30N Baseline configuration tested in the University of Bristol's low-speed large wind tunnel, validated against the results from the D5 open test section at an angle of attack $\alpha = 8°$ [28].

tunnel at the University of Bristol follows the same trend as that of the open test section results from Li *et al.* [28]. The results presented in Fig. 5(b) show the pressure coefficient around the Baseline configuration at a chord-based Reynolds number of $Re_c = 7.0 \times 10^5$ along with the published test results from Li *et al.* [28] at a chord-based Reynolds number of $Re_c = 1.71 \times 10^6$ for the angle of attack $\alpha = 8°$. The Baseline results validate well with the open test section results from Li *et al.* [28]. Therefore the following aerodynamic results presented in this study cannot be compared with ideal free flight conditions due to the considerable effects of the flow deflection and wind tunnel sidewall interference. The aim of this section is to demonstrate the aerodynamic characteristics of the H-SCF and SCF configurations relative to the Baseline.

3.2. Aerodynamic force measurements

The aerodynamic lift and drag measurement results for the MDA 30P30N airfoil with different cove fillers at the free-stream velocity of $U_\infty = 40$ m/s, corresponding to a chord-based Reynolds number of $Re_c = 9.3 \times 10^5$ are presented in Fig. 6. The tests were carried out for the angles of attack ranging from $\alpha = 0°$ to $18°$ with an increment of $2°$. The lift and drag coefficients (C_L and C_D) for the Baseline, H-SCF, SCF, and the SCF-FCF configurations are presented in Fig. 6. The C_L results show an insignificant difference between the cases for all the presented angles of attack. The C_D results, on the other hand, show that the SCF-FCF configuration produced the highest C_D compared to the Baseline and all the other configurations at all the angles of attack. The H-SCF configuration has the least C_D relative to the Baseline and the other configurations for all the tested angles of attack. The C_D values for the SCF case is the same as that of the Baseline. Therefore, it can be inferred that the use of slat cove fillers have a more pronounced effect on the drag than the lift generated by the airfoil.

The results for the lift-to-drag ratio and the drag polar curves for the Baseline, H-SCF, SCF, and the SCF-FCF configurations are presented in Fig. 7. The lift-to-drag ratio (C_L/C_D)

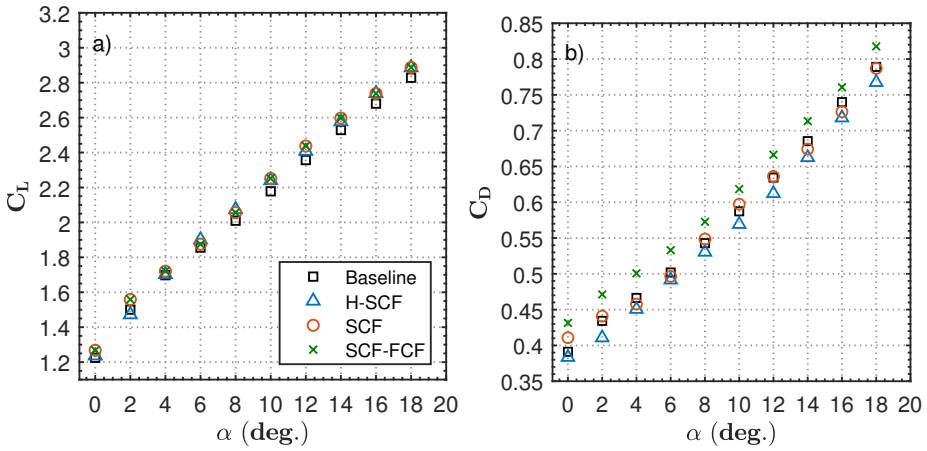

Figure 6: Lift and drag coefficients for the MDA 30P30N airfoil with various cove fillers at chord-based Reynolds number $Re_c = 9.3 \times 10^5$.

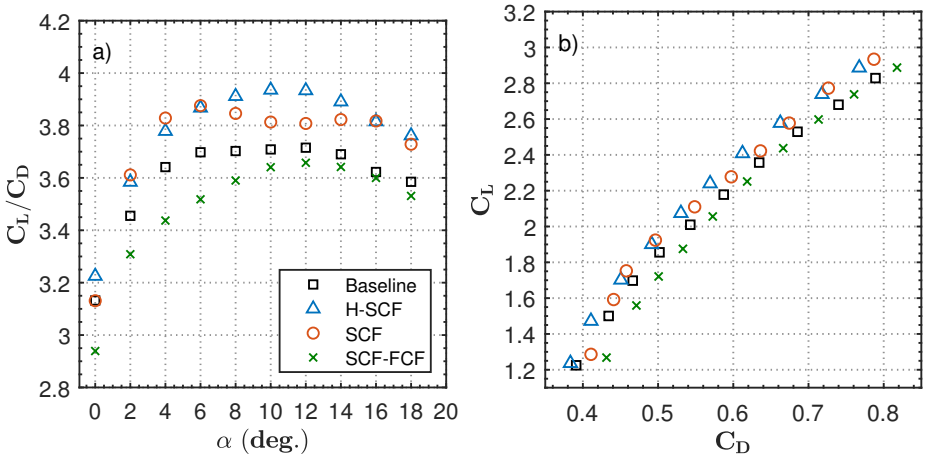

Figure 7: Lift-to-drag ratio and the drag polar plots for the MDA 30P30N airfoil with various cove fillers at chord-based Reynolds number $Re_c = 9.3 \times 10^5$.

results show a significant difference between the different configurations. The H-SCF produces a higher C_L/C_D relative to the Baseline and the SCF-FCF configuration. For the SCF configuration with a large cove filler, the C_L/C_D values remain the same as that of the best performing H-SCF between $\alpha = 0°$ to $8°$ and $16°$ to $18°$. The highest change in C_L/C_D value was observed for the H-SCF case relative to the Baseline between $\alpha = 8°$ and $14°$ with an average increase of $\Delta C_L/C_D \approx 0.214$ ($\approx 5.4\%$). The largest difference in C_L/C_D is found at $\alpha = 6°$ between the H-SCF and SCF-FCF cases, with a $\Delta C_L/C_D = 0.358$. The drag polar curve results in Fig. 7b show the C_D in the abscissa and C_L in the ordinate for increasing angles of attack. The results clearly show that the H-SCF has the least drag and highest lift for all the presented angles of attack, while the SCF-FCF has the highest drag and least lift compared to the other configurations.

3.3. Pressure coefficient distribution

The pressure coefficient (C_p) distribution, calculated from the static pressure measurements acquired along the mid-span of the high-lift device, for various chord-based Reynolds

numbers, $Re_c = 4.9 \times 10^5, 7.0 \times 10^5, 9.3 \times 10^5$ and 1.1×10^6, at the angle of attack $\alpha = 12^\circ$ is presented in Fig. 8. The results show that the changes in C_p distribution over the slat and main-element are insignificant for the tested Reynolds numbers except for the flap suction peak. The suction peak (C_p) of the main-element showed an increase of only 1.5% for $Re_c = 9.3 \times 10^5$ relative to $Re_c = 4.9 \times 10^5$, whereas the changes on the suction peak of the flap were up to 15% higher for $Re_c = 9.3 \times 10^5$ and 20% higher for $Re_c = 1.1 \times 10^6$ relative to the $Re_c = 4.9 \times 10^5$. Valarezo [51, 52] showed that the effects of Reynolds number on the lift of multi-element airfoil was very evident for flow conditions below $Re_c = 4 \times 10^6$. They also showed a considerable increase in the maximum lift between $Re_c = 2 \times 10^6$ and 9×10^6 at a Mach number of 0.2. The effects of Reynolds number and its significance on the lift of high-lift airfoils along with its increased effects on the suction peak of the main-element and flap were shown by Chin *et al.* [53]. As seen in the previous studies the effect of Reynolds number on the suction peaks can also be seen in the present study but only with a marginal magnitude. The results presented in this study are for a considerably lower Reynolds number range compared to the real flight conditions as this study is focused primarily on the further understanding of the fundamental flow physics of the slat and slat cove fillers. To gain a better insight into the slat cove filler technology in real flight conditions, further studies at much higher Reynolds numbers will be required.

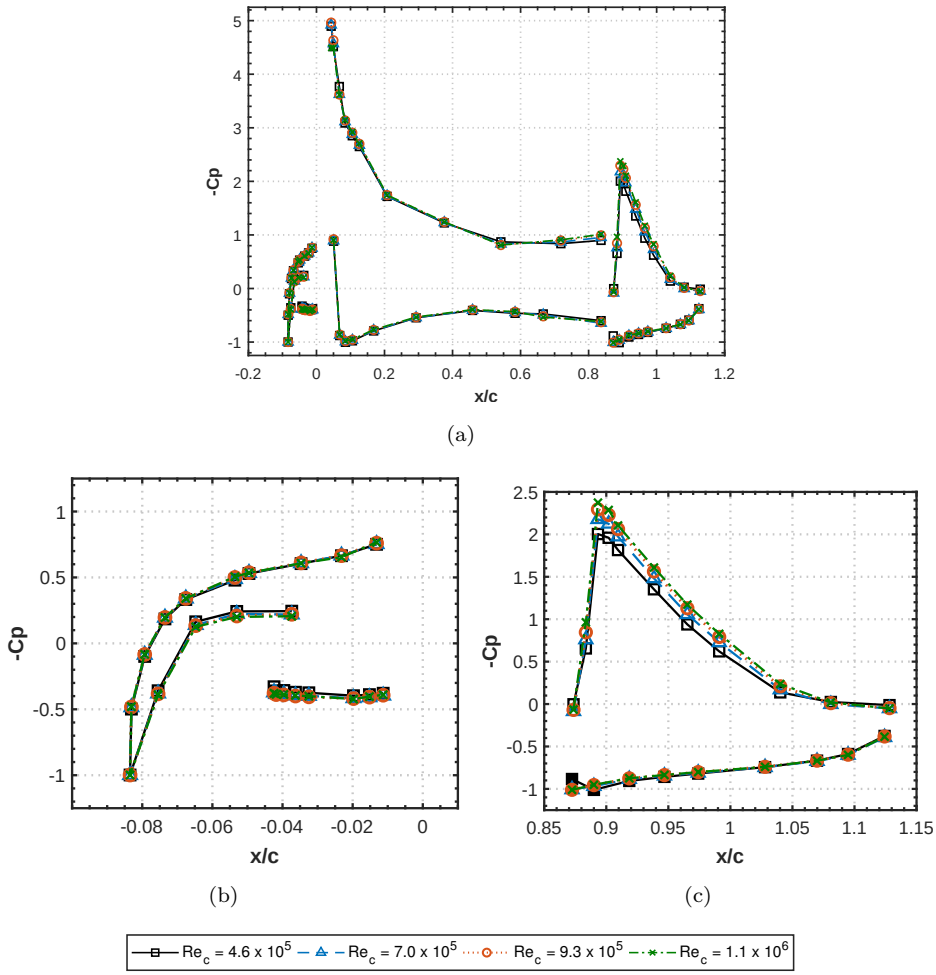

Figure 8: (a) Pressure coefficient distribution over 30P30N Baseline airfoil for various chord-based Reynolds numbers at angle of attack $\alpha = 12°$, (b) close-up view of the slat and (c) close-up view of the flap

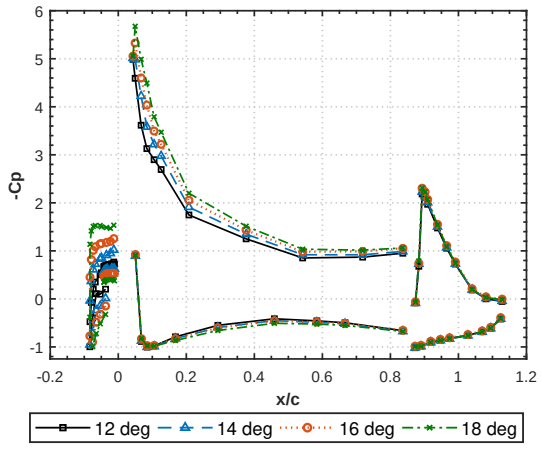

Figure 9: Pressure coefficient distribution over 30P30N Baseline airfoil for various angles of attack at a free-stream velocity of $U_\infty = 30$ m/s, $Re_c = 7.0 \times 10^5$.

The pressure coefficient distribution for the Baseline at the angles of attack $\alpha = 12°, 14°,$

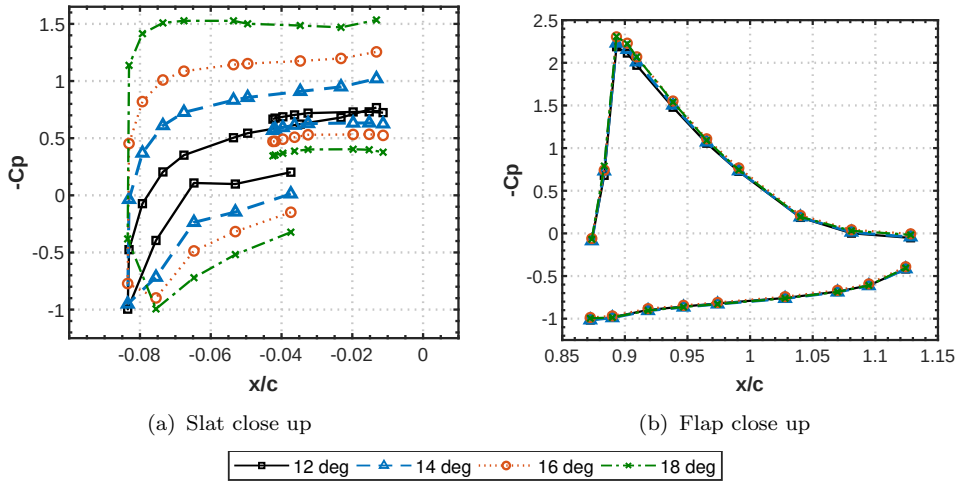

(a) Slat close up

(b) Flap close up

Figure 10: Pressure coefficient distribution over 30P30N Baseline airfoil around the slat and flap region for a free-stream velocity of $U_\infty = 30$ m/s, $Re_c = 7.0 \times 10^5$.

16° and 18° are presented in Fig. 9. The increase in the C_p distribution on the suction side of the main-element as the angle of attack is increased is evident. The loading on the slat and main-element increases with the increase in the angle of attack. The increased suction peak on the main-element at higher angles of attack is believed to be due to the higher velocity through the slat gap as the angle of attack is increased. The suction peak on the upper surface of the main-element increases up to $\approx 1\%$, 6.8% and 14% for $\alpha = 14°$, 16° and 18°, respectively, relative to $\alpha = 12°$. The suction peak on the upper surface of the flap increases up to $\approx 5.6\%$ for $\alpha = 18°$ relative to $\alpha = 12°$.

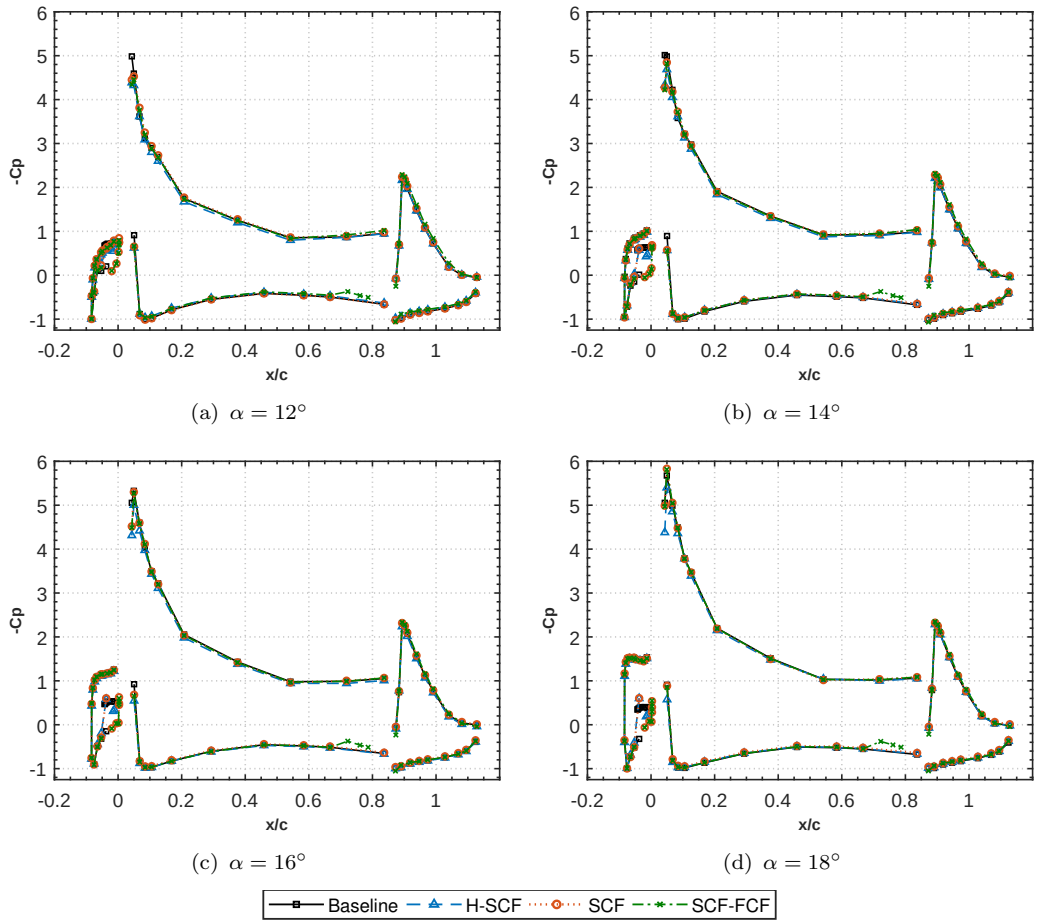

Figure 11: Pressure coefficient distribution over 30P30N airfoil with slat modifications, at various angles of attack for a free-stream velocity of $U_\infty = 30$ m/s, $Re_c = 7.0 \times 10^5$.

Figures 11 and 12 show the pressure coefficient C_p results for the Baseline, H-SCF, SCF and SCF-FCF configurations at the angles of attack $\alpha = 12°, 14°, 16°$ and $18°$ for a free-stream velocity of $U_\infty = 30$ m/s. The results in Fig. 11 show that the modifications on the slat, such as the application of H-SCF and SCF, affect the suction peak on the main-element of the airfoil. The Baseline case has the highest suction peak for all the presented angles of attack. The C_p suction peak on the main-element at location $x/c = 0.043$ was reduced by approximately 12% at $\alpha = 12°$ and approximately 15% at $\alpha > 12°$ for the H-SCF, SCF and the SCF-FCF cases relative to the Baseline case. The results for the slat in Fig. 12 show that the C_p on the pressure side changes quite significantly for the H-SCF and SCF configurations as the angle of attack is increased. The suction peak near the slat cusp is decreased for the H-SCF and SCF configuration relative to the Baseline by up to 40% for the angle of attack $\alpha = 12°$. This is due to the absence of the sudden pressure gradient and the increased velocity that arises as a result of the streamlined profile of the cove fillers. The C_p measurements over the flap for the presented angles of attack remains unchanged for the Baseline, H-SCF and SCF configurations. The results for the SCF-FCF configuration show an increase of up to $\approx 20\%$ in the C_p on the pressure side of the main-element at the location of the flap cove filler between $x/c \approx 0.6$ and 0.8. The SCF-FCF results over the flap at the

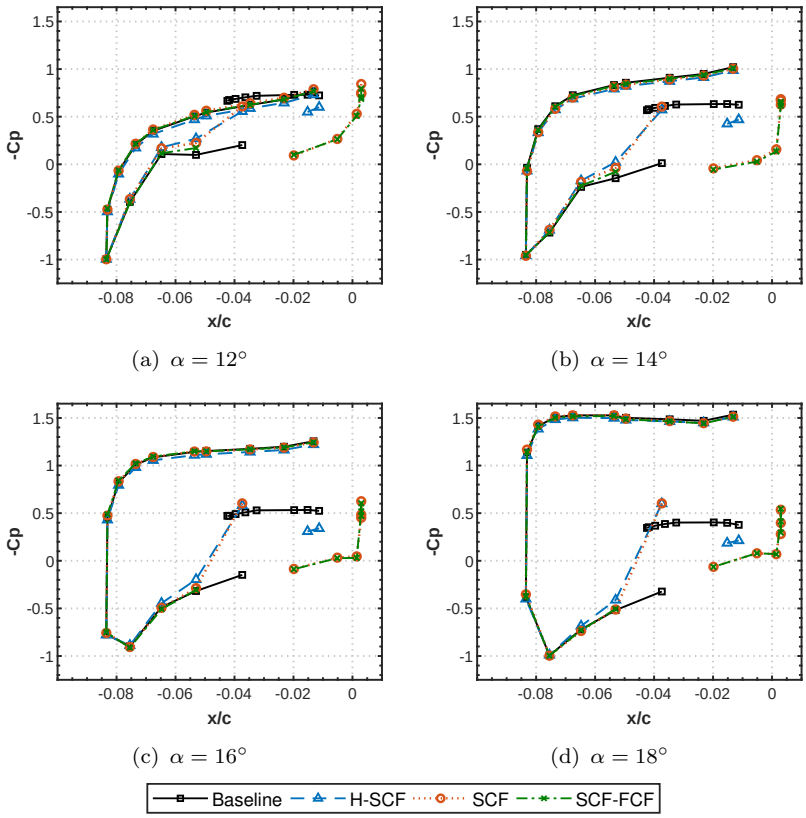

Figure 12: Pressure coefficient distribution over 30P30N airfoil with slat modifications, at various angles of attack for a free-stream velocity of $U_\infty = 30$ m/s, $Re_c = 7.0 \times 10^5$.

suction peak location $x/c = 0.90$ is $\approx 5\%$ higher for the SCF-FCF configuration relative to the Baseline.

4. Aeroacoustic results

High-lift devices are one of the dominant components of the airframe noise. The slat noise is much of interest to researchers due to its complex tonal and broadband noise generation mechanisms [24–31]. The noise generated by high-lift devices largely varies with respect to the geometry in terms of tonal noise frequency range and tonal peak location. Emphasizing on the similarities in the tonal noise seen in rectangular cavities, the slat cove region can be considered as an open cavity. Previous studies [17, 22, 27, 54, 55] have shown that the feedback mechanism between the unsteady vortices emanating from the slat cusp and the trailing edge acts as a resonator. The noise generated in cavities are due to the flow induced cavity oscillations and the multiple acoustic scales arise due to the vortical disturbances driving the oscillations. Rossiter [56] showed that the discrete frequencies in rectangular cavities are due to the oscillations influenced by the acoustic feedback from the shear layer impingement region. The study also proposed an empirical formula to predict the tonal frequencies in rectangular cavities. Kolb *et al.* [17] applied an improved version of the Rossiter equation [56, 57] on the slat noise mechanism and showed that the analytical Rossiter frequencies agreed well with the measured experimental tonal peaks. Terracol *et al.* [22] further sim-

plified the Rossiter equations [56, 57] and matched the slat cove tonal frequencies for the FNG Airbus geometry F16. Pascioni and Cattafesta [27] applied the simplified equation by Terracol *et al.* [22] on a 30P30N geometry and showed that the tones and their harmonics can be accurately predicted. These studies have shown the robustness of the Rossiter equations to predict the tonal noise generated by a slat.

The discrete tonal frequencies due to the flow interaction with the slat, based on Terracol's study [22], can be predicted from

$$f_n = n\frac{U_\infty}{L_a}\left(\frac{1}{M+\eta_l/\kappa_v}\right). \tag{1}$$

A simplified schematic of the parameters used in Eq. 1 by Terracol *et al.* [22] are shown in Fig. 13 and the parameters used in the current study are listed in Table 3. The equation is found to be highly sensitive to the shear layer path length (L_v) and acoustic path length (L_a). The flow field, i.e. local flow velocity, data required for this prediction model were acquired from the PIV measurements by from the authors' previous studies [1, 2].

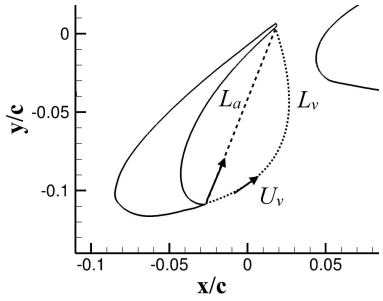

Figure 13: Simplifed schematic of the tonal frequency prediction model by Terracol *et al.* [22].

α	Angle of attack	14°	18°	units
L_v	Shear layer path length	0.048	0.037	m
L_a	Acoustic path length	0.0405	0.035	m
U_v	Shear layer convection velocity	23.4	19.5	m/s
U_∞	free-stream velocity	30	30	m/s
M	free-stream Mach number	0.09	0.09	-
κ_v	$= U_v/U_\infty$	0.78	0.65	-
η_l	$= L_v/L_a$	1.196	1.060	-

Table 3: Parameters used for tonal peak frequency prediction in the present study.

4.1. Test conditions

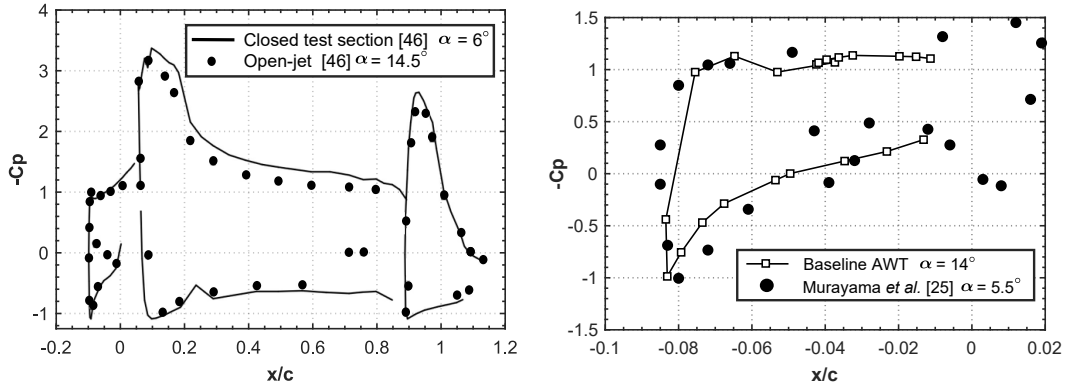

(a) (b)

Figure 14: (a) A comparison of the pressure distribution for the F15 high-lift system in an open-jet test section at the angle of attack of $\alpha = 14.5°$ to that in a closed test section at the angle of attack of $\alpha = 6°$, extracted from Manoha *et al.* [46]. (b) Pressure distribution for the 30P30N Baseline configuration at a geometrical angle of attack $\alpha = 14°$ in the open-jet aeroacoustic wind tunnel facility at the University of Bristol compared to that of Murayama *et al.* [21] in a closed test section at the angle of attack $\alpha = 5.5°$.

The acoustic measurements were carried out in the open-jet aeroacoustic wind tunnel facility at the University of Bristol [43, 44]. The effects of carrying out measurement in an open-jet facility must be considered for high-lift airfoils as they cause high flow deflection due to their high camber and the circulation region around the high-lift airfoil [46]. Manoha and Pott-Pollenske [46] have shown that the difference between the corrected and geometric angles of attack for high-lift airfoils in open-jet configuration can be as high as 8.5°, as shown in Fig. 14(a), extracted from [46]. With regard to matching the high-lift airfoil pressure distribution from different tests, they also argued that the high-lift airfoils should generate the same noise levels if their slat pressure distribution matched. In order to estimate the corrected angle of attack in the present tests, the measured static pressure distribution from the open-jet anechoic wind tunnel were compared with the benchmark data-set from Murayama *et al.* [21]. The results presented in Fig. 14(b) show the comparison of the slat pressure coefficient for the tested Baseline configuration with the benchmark data-set [21]. The results of the Baseline configuration at the geometric angle of attack of $\alpha = 14°$, and Reynolds number of $Re_c = 7.0 \times 10^5$, are compared with the angle of attack of $\alpha = 5.5°$, at $Re_c = 1.71 \times 10^6$ from Murayama *et al.* [21], see Fig. 14(b). The results of the pressure coefficient distribution around the slat region can be observed to agree well with those of Murayama *et al.* [21]. The comparative results show that the angle of attack correction for the current study is also about 8.5°, similar to Manoha and Pott-Pollenske [46]. Though not presented here, the results of the far-field individual microphone measurements of the Baseline configuration at $\alpha = 14°$ have also been validated with the benchmark data-set available from Pascioni *et al.* [27] and Li *et al.* [28], with an angle of attack correction of 8.5°. The aeroacoustic results presented in the following sections are presented for the geometric angles of attack $\alpha = 14°$ and 18° in the open-jet aeroacoustic wind tunnel facility.

4.2. Far-field spectral levels

Far-field noise measurements were carried out in order to assess the noise generated from the Baseline, H-SCF, and SCF configurations. The sound pressure level measured from a far-field microphone at 90° above the slat trailing edge for the angle of attack $\alpha = 14°$ and 18° at the free-stream velocity of $U_\infty = 30$ m/s is shown in Fig. 15. The results show that the background noise of the aeroacoustic facility is well below the high-lift airfoil noise levels. While the results for the baseline 30P30N airfoil show the discrete narrowband peaks, typical of the noise signature from such high-lift devices, the far-field noise results of the H-SCF and SCF configuration do not demonstrate such tonal behavior. The SCF configuration at the angle of attack $\alpha = 18°$ clearly shows a reduction in the noise levels over the entire frequency range. Significant noise reduction of up to 8 dB at low to mid-frequency range ($St_s < 5$) is observed for the SCF configuration compared to the Baseline and H-SCF cases. The generation of the tonal peaks and the mechanisms driving them will be discussed in detail in the following sections.

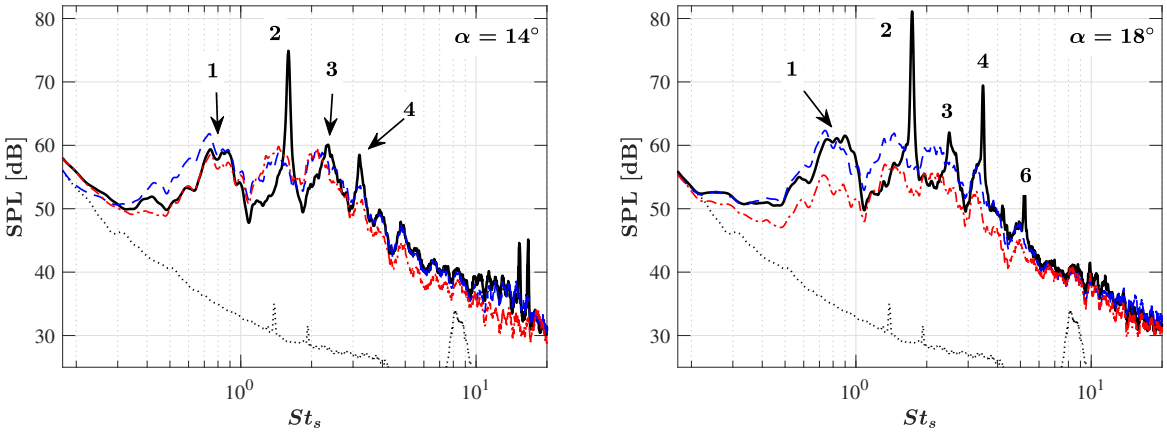

Figure 15: Far-field noise spectra for microphone at 90° and 1.75 m above the slat trailing edge for Baseline ——, H-SCF – –, SCF —·— and Background noise ·····. The resonance modes are listed in Table 4.

The Far-field directivity plots from the pressure side elevation angles for the Baseline, H-SCF, and SCF configurations at different slat based Strouhal number ($St_s = f \cdot c_s/U_\infty$) are presented in Fig. 16. The results are plotted for the angles of attack $\alpha = 14°$ and 18°, for a free-stream velocity of $U_\infty = 30$ m/s, corresponding to a chord-based Reynolds number of $Re_c = 7.0 \times 10^5$. The results are shown for the selective Strouhal numbers based on the narrowband peaks observed at the far-field spectral levels in Fig. 15. At first glance, it is evident that the application of the H-SCF and SCF does not influence the overall directivity shape for the presented range of Strouhal numbers compared to the Baseline case. For $\alpha = 14°$, at St_1, the acoustic amplitude of the directivity results remains unchanged for the H-SCF and SCF configurations compared to the Baseline case but a reduction of up to 10 dB is observed at $\alpha = 18°$ for the SCF configuration over the whole polar angles. The reduction in the spectral levels for the cove filler configurations for the modes $St_{2\&4}$ are substantial, with a reduction of up to 20 dB at both the presented angles of attack. The noise level results show a significant reduction for the H-SCF and SCF cases relative to that of the Baseline case at $\alpha = 18°$, at all frequencies.

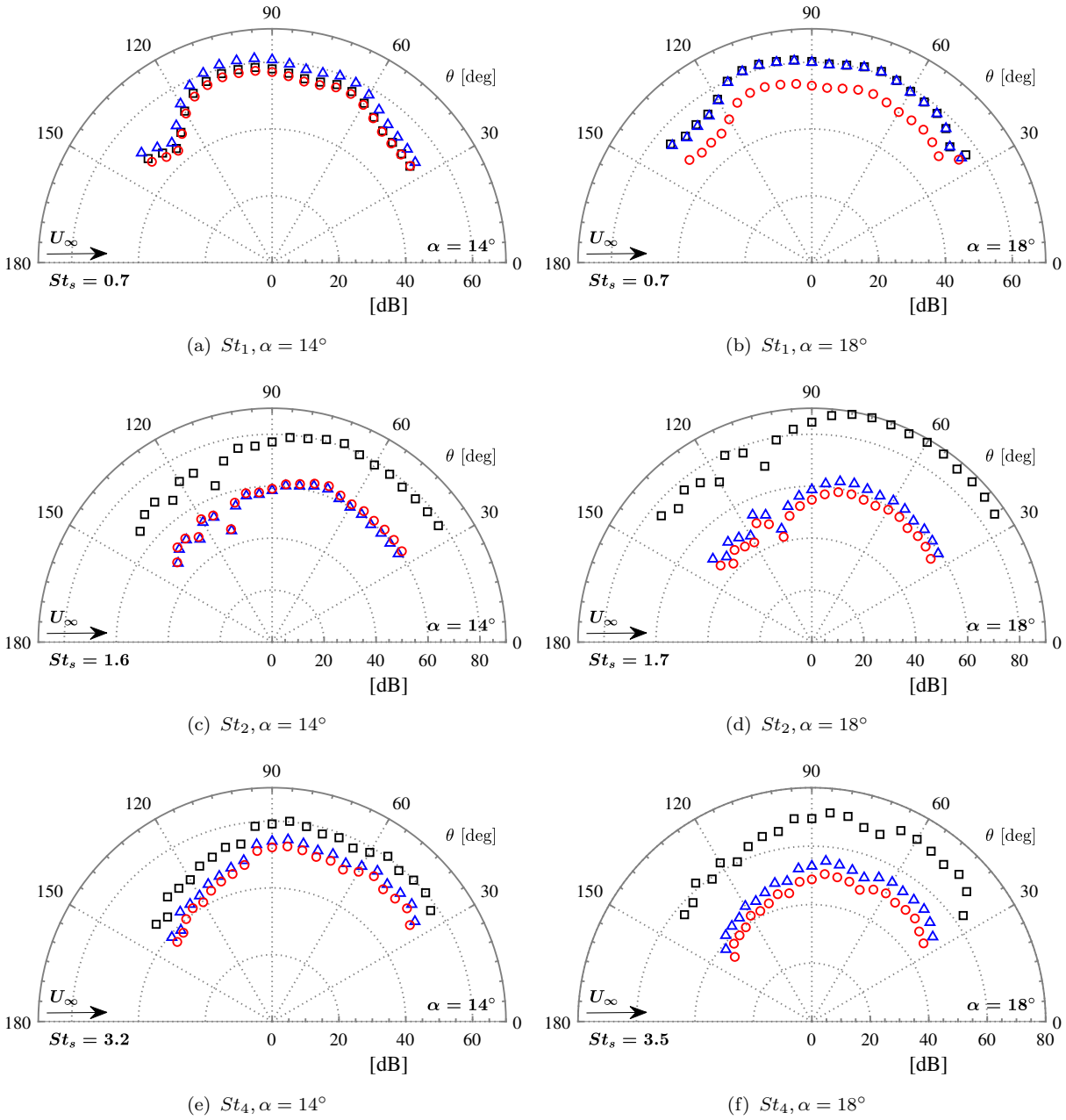

Figure 16: Directivity for the different configurations at different slat based Strouhal number, for Baseline □, H-SCF △ and SCF ○.

The overall sound pressure levels (OASPL) for the different configurations are shown in Fig. 17. The overall sound pressure level was resolved for a frequency range from $f = 100$ Hz to 6300 Hz. The results show that the applications of the H-SCF and SCF reduces the overall noise level by about 2-3 dB at $\alpha = 14°$ and a significant reduction of up to 10 dB at the higher angles of attack ($\alpha = 18°$) compared to that of the Baseline case, particularly at locations upstream of the slat trailing edge.

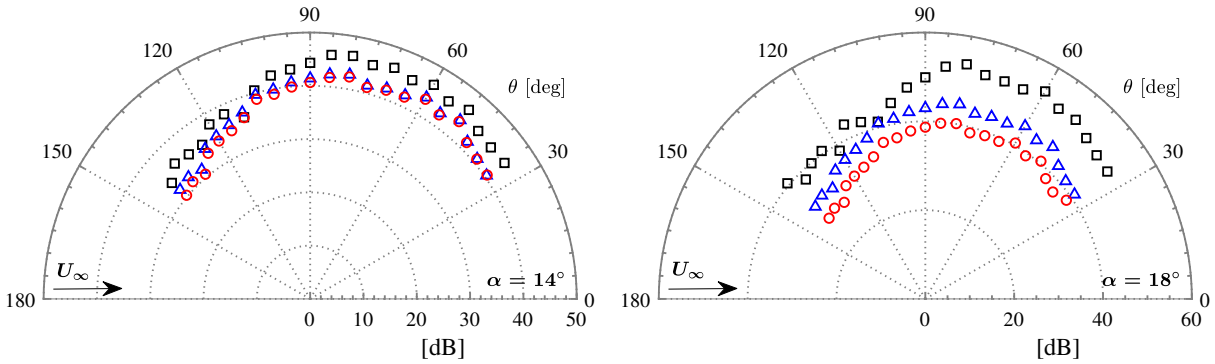

Figure 17: Overall sound pressure level calculated from the far-field microphones, for Baseline □, H-SCF △ and SCF ○.

4.3. Near-field spectral levels

Near-field unsteady pressure measurements were performed to gain an insight into the noise generation mechanism of the slat. The unsteady surface pressure measurements were acquired at various spanwise locations on the surface of the main-element of the high-lift airfoil. The measurements were carried out using 5 surface-mounted pressure transducers, which are detailed in Table 2. The data were acquired for 16 seconds and sampled at 40 kHz. Even though the measurements were carried out for the angles of attack $\alpha = 12°$, 14°, 16° and 18°, the results here are presented only for the angles of attack $\alpha = 14°$ and 18°, for the purpose of brevity. The sound pressure levels are presented in terms of the slat based Strauhal number ($St_s = f \times c_s/U_\infty$). From the aeroacoustic study carried out by Murayama *et al.* [21], it was seen that the surface mounted pressure transducers on the main-element can be used to accurately predict the slat tones and can also provide some useful information about the broadband energy content of the flow structures within the slat cove. The results from the unsteady surface pressure measurements from the transducer M1 at the leading edge of the main-element are shown in Fig. 18. The tonal characteristics of the wall pressure spectra indicate the presence of cavity oscillations. The wall pressure fluctuation spectra results for the Baseline in Fig. 18 show multiple distinct narrowband peaks for all the tested angles of attack with varying intensities, characterizing cavity oscillations. Some of the tonal peaks were also observed in the far-field noise measurements. The tonal peaks are numbered in Fig. 18 and are listed in Table 4.

As discussed earlier, the tonal peaks observed are due to the flow-acoustic coupling which leads to resonance as all of them could be accurately predicted by the simplified Rossiter mode equation. At the angle of attack $\alpha = 14°$, the pressure spectra results show three distinct peaks $St_{1,2,3} = 0.885, 1.596$ and 3.203. These are the first three Rossiter modes and the fourth mode, $St_4 = 3.203$ was also observed but with low intensity. The first mode (St_1) predicted by the analytical formula is not distinctly seen in the experiments as it lies within the spectral hump seen at low-frequency $0.5 < St_s < 1$. For the angle of attack $\alpha = 18°$, at the first glance, the results of the Baseline case appear chaotic with multiple peaks but the observed discrete tonal peaks are the first 14 Rossiter modes, as predicted by Eq. 1 (see Table 4). The multiple peaks seen here also depict harmonic behavior and possess an algebraic relationship amongst themselves. A cascading effect in the modes is seen through the entire mid to high frequency range i.e. $St_4 = 2St_2$, $St_5 = St_3 + St_2$, $St_6 = 3St_2$ and

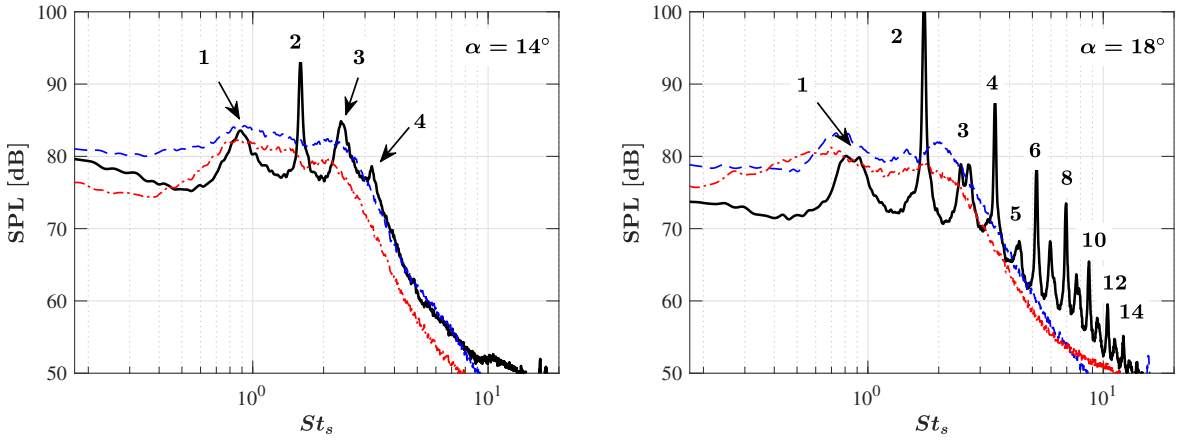

Figure 18: Near-field noise spectra for the surface transducer M1 ($x = 22.414$ mm) for Baseline ——, H-SCF – – and SCF —·—. The associated modes St_n are listed in Table 4.

	$\alpha = 14°$					$\alpha = 18°$				
No.	St_n	St_s	Description	Experiment f (Hz)	Analytical f (Hz)	St_n	St_s	Description	Experiment f (Hz)	Analytical f (Hz)
1	St_1	0.8855	mode 1	506	456.3	St_1	0.896	mode 1	512	498.1
2	St_2	1.596	mode 2	912	912.6	St_2	1.733	mode 2	990.29	996.2
3	St_3	2.373	mode 3	1356	1368.9	St_3	2.481	mode 3	1417.71	1494.3
4	St_4	3.203	$= 2St_2$	1830.29	1825.2	St_4	3.468	$= 2St_2$	1981.71	1992.5
5	-	-	-	-	-	St_5	4.393	$= St_3 + St_2$	2510.29	2490.6
6	-	-	-	-	-	St_6	5.215	$= 3St_2$	2980	2988.7
7	-	-	-	-	-	St_7	5.96	$= St_5 + St_2$	3405.71	3486.8
8	-	-	-	-	-	St_8	6.958	$= 4St_2$	3976	3984.9
9	-	-	-	-	-	St_9	7.7	$= St_7 + St_2$	4400	4483
10	-	-	-	-	-	St_{10}	8.701	$= 5St_2$	4972	4981.2
11	-	-	-	-	-	St_{11}	9.482	$= St_9 + St_2$	5418.29	5479.3
12	-	-	-	-	-	St_{12}	10.44	$= 6St_2$	5965.71	5977.4
13	-	-	-	-	-	St_{13}	11.19	$= St_{11} + St_2$	6394.29	6475.5
14	-	-	-	-	-	St_{14}	12.18	$= 7St_2$	6960	6973.6

Table 4: The narrow-band frequencies observed for the Baseline case in the near-field and far-field measurements at angles of attack $\alpha = 14°$ and 18° and the labels in Figs. 15 and 18 are detailed.

$St_7 = St_5 + St_2$. The presence of such an algebraic relationship between the modes suggests the occurrence of nonlinear quadratic interaction between the Rossiter modes, which will be discussed in detail in Section 4.6. The magnitude of the tonal peaks also varies relatively for the Baseline case, especially with the peaks of the even modes having higher magnitude compared to the consecutive odd modes. It is notable that the first Rossiter mode is concealed within the spectral hump $0.5 < St_s < 1$. The results are indicative that the source of the spectral hump might not be solely due to the Rossiter modes. The Rossiter modes are due to the flow-induced oscillations and acoustic feedback mechanism since the modes 2-14 observed have a distinct narrowband peak. The source of this spectral hump has not yet been identified in the previous studies.

The results of the H-SCF and SCF configurations for both the presented angles of attack do not show any indication of the above discussed tonal peaks. The wall pressure spectra at the angle of attack $\alpha = 14°$, for the H-SCF, show an increase of about 5 dB at low-frequency range $St_s > 0.8$. The presence of the semi-cavity in the case of H-SCF gives rise

to two spectral humps at $St_s = 0.6$ and 2 at the angle of attack $\alpha = 18°$. Even though the H-SCF configuration has a semi-cavity the tonal peaks are not observed in the near and far-field measurements. The two spectral humps at $St_s = 0.6$ and 2 at the angle of attack $\alpha = 18°$ might be due to the semi-cavity as they are not observed in the SCF case. The SCF configuration shows a reduction at low-frequency range for the angle of attack $\alpha = 14°$ and increased levels for the same range of frequencies at the angle of attack $\alpha = 18°$. The tonal peaks are also absent for the SCF configuration in the near-field measurements. The increased spectral levels seen in the near-field surface pressure measurements for the SCF are absent in the far-field measurements in Fig.15, which implies that the increased spectra in the near-field are due to the non-propagating hydrodynamic energy field within the slat and main-element. The results for the H-SCF case show a spectral hump at St_1, the same as that of the Baseline irrespective of the reduced slat cove size. This again confirms that the St_1 and the broadband hump in this region might be different in nature compared to the dominant even-numbered modes seen in the Baseline case. Some of the discrete narrowband peaks seen at high-frequency were not seen in the far-field measurements as they fall below the broadband content of the noise radiated to the far-field observer.

4.4. Spanwise coherence

The spatial coherence scales are used to determine the extent of the pressure wave interference and this can help us better understand the hydrodynamic field and radiated noise. An experimental study of the spanwise coherence at the slat vicinity for the 30P30N high-lift airfoil was shown by Murayama *et al.* [21]. Complementing the previous study, the current study has provided the spanwise coherence results for the Baseline, H-SCF and SCF configurations, which can potentially improve our understanding of the flow structures at the slat region and the leading-edge of the main-element. The spatial coherence scales are used to determine the extent of the pressure wave interference and this can help us better understand the hydrodynamic field and the radiated noise. The spanwise coherence calculates the phase correlation between two different spanwise pressure transducers averaged over time.

The spanwise coherence calculates the phase correlation between two different spanwise pressure transducers averaged over time. The spanwise coherence between the surface pressure transducers can be obtained using the following equation,

$$\gamma^2_{p_i p_j}(f, \Delta z) = \frac{\mid \Phi_{p_i p_j}(f) \mid^2}{\Phi_{p_i p_i}(f)\Phi_{p_j p_j}(f)} \quad \text{for } p_i = \text{ M1 and } p_j = \text{ M1, M2.....M5,} \tag{2}$$

where M1-M5 are the unsteady pressure transducers mounted on the leading-edge of the main-element and their locations are provided in Table 2. The spanwise coherence between the reference transducer M1 and the other spanwise located surface transducers M2, M3, and M5, for the three configurations are presented in Fig. 19. For the smallest lateral spacing $\Delta z/c_s = 0.07$ (between M1 and M2) the results show high coherence for all the cases at both the angles of attack over the whole frequency range. The coherence results for the Baseline and H-SCF cases (Fig. 19 (c)) for the spanwise spacing of $\Delta z/c_s = 0.22$ (between M1 and M3) show coherence reduction in the high-frequency range but high coherence levels at the tonal peaks. At the largest separation distance, $\Delta z/c_s = 0.81$ (between M1 and M5) the coherence for all the frequencies is almost zero, except for the tonal peaks observed in the surface pressure spectra (see Fig. 18) for both the angles of attack. The results at the angle of attack $\alpha = 18^\circ$ show that except for the tonal peaks, over the broadband range of the spectra, the three configurations have similar spanwise coherence indicating that they all have similar three-dimensional flow structures. The most notable aspect of the coherence results is that the spectral hump at St_1 shows a high level of coherence for all the presented separation distances and all configurations. It is interesting that high level of coherence for the broadband spectral hump at low frequencies is seen for both the cove filler H-SCF and SCF configurations (see Fig. 19 (c)). Even for the largest $\Delta z/c_s = 0.81$, a remnant of the phase correlation of the pressure waves are seen at about St_1, with values of up to $\gamma^2_{p_i p_j} \approx 0.2$ for the H-SCF and SCF cases. This is indicative of the fact that the source of the spectral hump is not quite as that of the Rossetier modes.

In order to estimate the noise generated through the interaction of advecting pressure in the vicinity of the airfoil, the spanwise correlation length of the wall pressure fluctuations were calculated. The spanwise correlation length of the flow structures and the local hydrodynamic field can be calculated using the following equation,

$$\Lambda_\gamma(f) = \int_0^\infty \gamma_{p_i p_j}(f, \Delta z) d\Delta z. \tag{3}$$

The length scale (Λ_γ) as a function of frequency is calculated using the spanwise coherence results (γ) between the surface pressure transducers and are presented in Fig. 20. For the angle of attack $\alpha = 14°$, the results show two distinct spectral humps for the length scales for all the configurations. The Baseline and the H-SCF results follow the same trend with similar length scales but with the absence of the tonal peaks for the H-SCF configuration. The SCF case shows slightly increased length scales relative to the Baseline and the H-SCF. At the angle of attack, $\alpha = 18°$, the three configurations possess the same broadband trend at mid to high-frequencies ($St_s > 1$). The length scales show the spectral hump for only the Baseline case at low-frequencies ($St_s < 1$). This shows that for the H-SCF configuration, even though the size of the cavity is reduced and the acoustic feedback mechanism that gives rise to the tonal behaviour has been eliminated, the spanwise correlation length remains the same as that of the Baseline airfoil. This behaviour was also observed by Zhang et al. [42].

The auto-correlation were calculated using the unsteady surface pressure, it is defined as,

$$R_{p_i p_i}(\tau) = \frac{\overline{p_i(t+\tau)p_i(t)}}{p^2_{i_{RMS}}}, \tag{4}$$

where p_i is the surface pressure, $p_{i_{RMS}}$ is the surface pressure root mean squared, τ is the time delay and the time average is represented by the overbar. The results of the auto-correlation of the surface pressure at the transducer location M1 at the angle of attack $\alpha = 14°$ and $18°$ are presented in Fig. 21, as a function of the normalized time delay $\tau^* = \tau U_\infty / c_s$. For the Baseline, at the angle of attack $\alpha = 14°$ the results exhibit a fast decaying periodic behavior. At the angle of attack $\alpha = 18°$ the results exhibit a slow decaying periodic behavior with a Gaussian shape with a low decay rate, which is suggestive of a strong vortex shedding. At the angle of attack $\alpha = 18°$, the distance between the two peaks in $R_{p_i p_i}(\tau)$ for the Baseline case corresponds to the vortex shedding frequency (τ^*_{vs}). The calculated time delay $\tau^*_{vs} = 0.5711$ corresponds to $St_{vs} = 1.75 \approx St_2$, which is the primary peak seen in power spectral plots (see Fig. 18) with the highest magnitude. The vortex shedding for the angle of attack $\alpha = 14°$ is not seen distinctly compared to $\alpha = 18°$. This is due to the lower energy of the vortex shedding frequency (see St_2 in Fig. 18) at angle of attack $\alpha = 14°$ (10 dB) compared to $\alpha = 18°$ (25 dB). The results of the H-SCF and SCF cases show a very weak periodic shape that decays instantaneously, indicating the absence of a strong vortex shedding for both the presented angles of attack. Even though the H-SCF configuration has half a cavity slat, its behavior is more similar to that of the SCF than the Baseline case.

To further understand the intensity of the noise radiated to the far-field and isolate the non-propagating hydrodynamic field, coherence between the surface pressure transducer M1 and the far-field microphone placed at 90° above the slat trailing-edge were carried out. The coherence was calculated using the following equation,

$$\gamma^2_{p_i p_j}(f) = \frac{\mid \Phi_{p_i p_j}(f) \mid^2}{\Phi_{p_i p_i}(f)\Phi_{p_j p_j}(f)} \quad \text{for } p_i = \text{ M1 and } p_j = \text{M}_{90°}, \tag{5}$$

where M1 is the reference surface pressure transducer and $M_{90°}$ is the far-field microphone at 90° above the slat trailing edge. The near- to the far-field coherence results are presented in Fig. 22. The results show high coherence at all tonal peaks that arise due to the Rossiter modes. The H-SCF and SCF cases show low coherence over the entire frequency range.

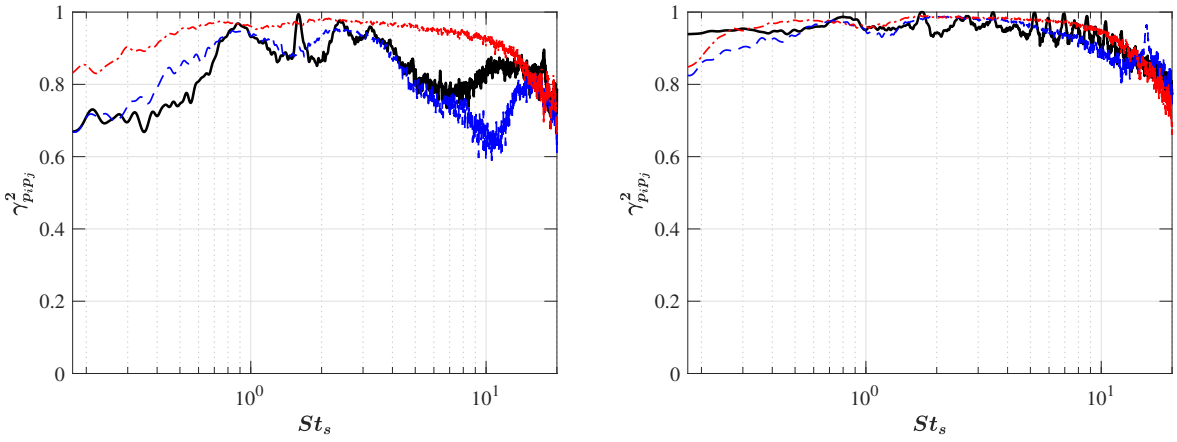

(a) $\alpha = 14°, \Delta z/c_s = 0.07$

(b) $\alpha = 18°, \Delta z/c_s = 0.07$

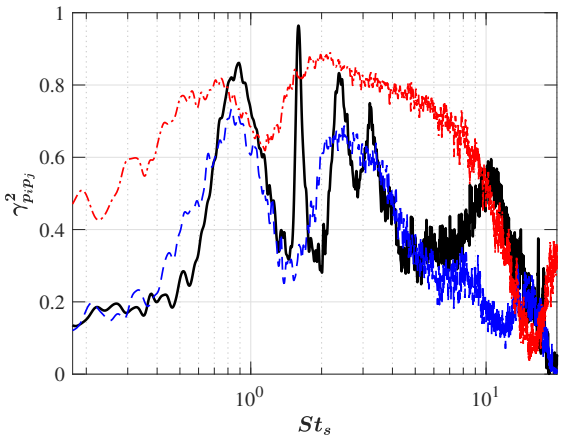

(c) $\alpha = 14°, \Delta z/c_s = 0.22$

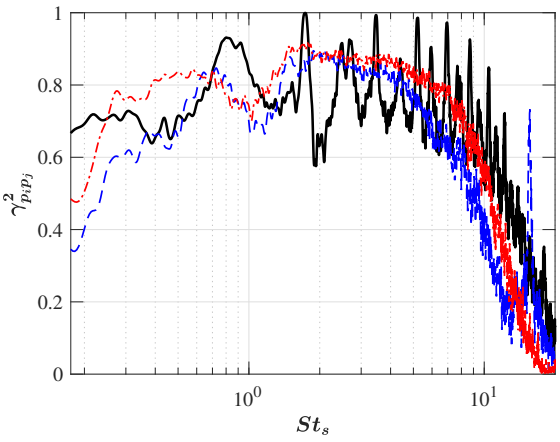

(d) $\alpha = 18°, \Delta z/c_s = 0.22$

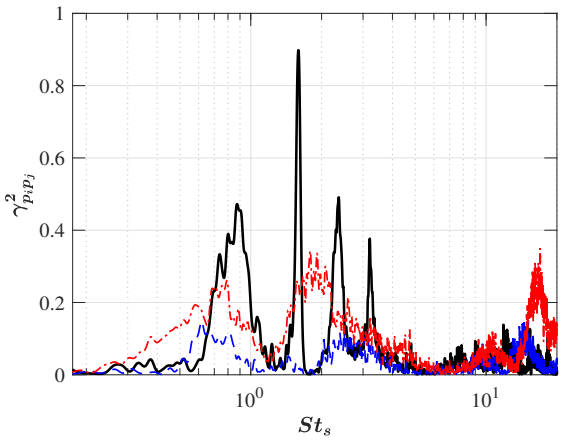

(e) $\alpha = 14°, \Delta z/c_s = 0.81$

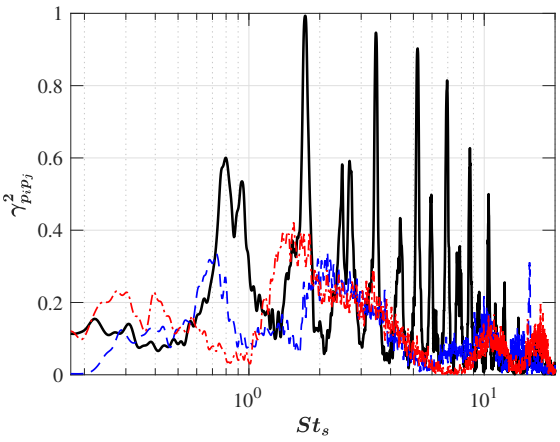

(f) $\alpha = 18°, \Delta z/c_s = 0.81$

Figure 19: Coherence between the reference transducer M1 and the other spanwise transducers M2-M5 (see Table 2), for Baseline ——, H-SCF – – and SCF —·—.

However, a noticeable spectral hump at $1 < St_s < 4$ with maximum coherence values up to

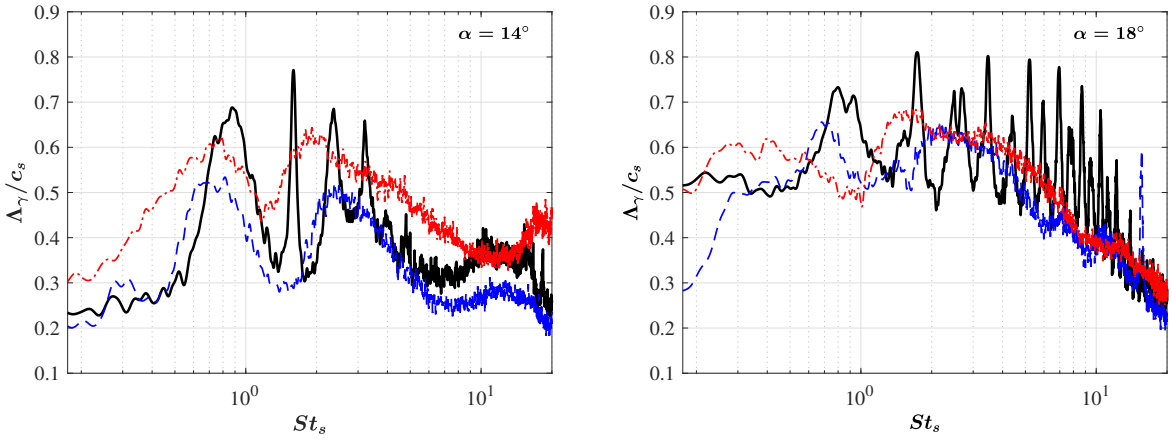

Figure 20: Spanwise coherence length scales based on the unsteady surface pressure measurement for Baseline ——, H-SCF – – and SCF —·—.

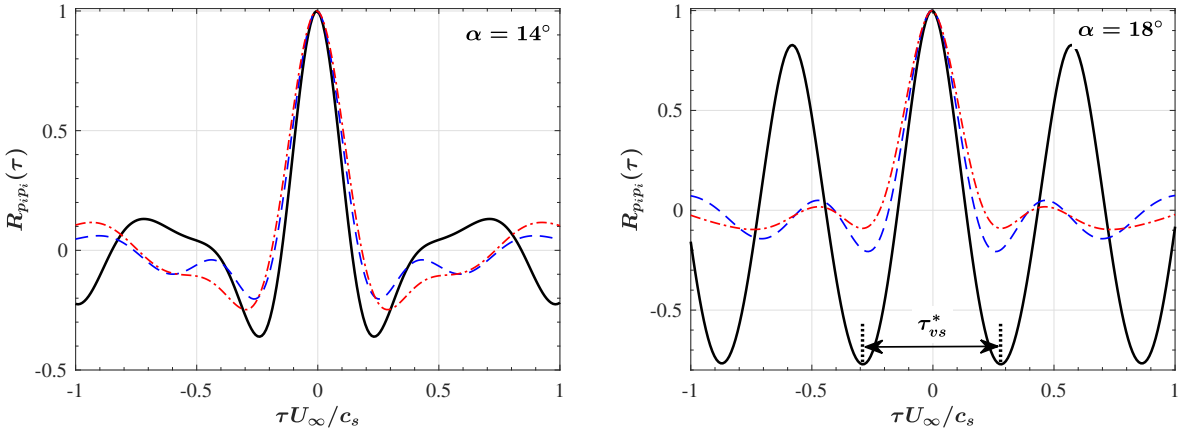

Figure 21: Auto-correlation of the surface pressure fluctuations at the near-field transducer location M1 for Baseline ——, H-SCF – – and SCF —·—.

$\gamma^2_{p_ip_{90°}} = 0.6$ for the H-SCF and SCF cases are seen. This increased coherence shows a feature that was not seen in both the near-field and far-field sound pressure level measurements.

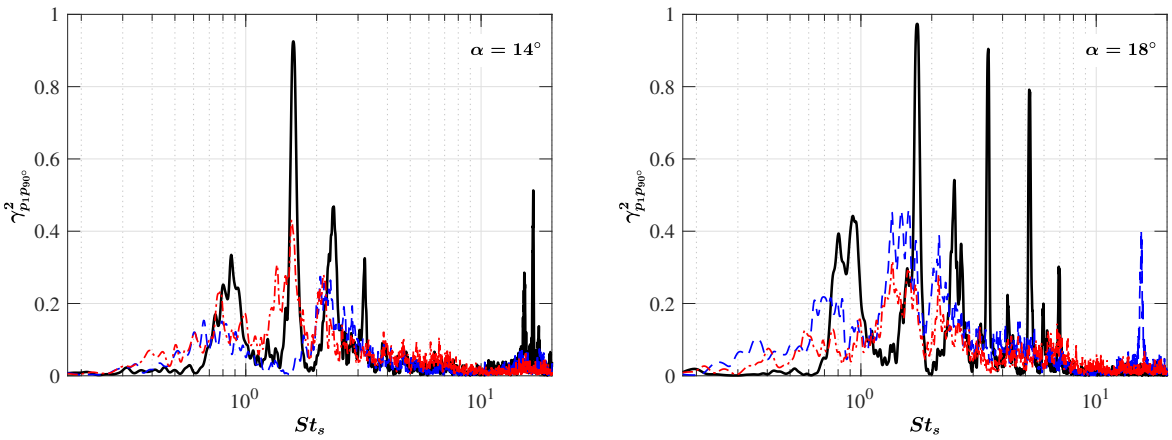

Figure 22: The coherence between the reference near-field surface pressure transducer M1 and the far-field microphone 90° above the trailing edge for Baseline ——, H-SCF — — and SCF —·—.

4.5. Continuous wavelet transform

The physical mechanism of the multiple distinct tones generated by the high-lift airfoils are suggested to be due to an amplitude modulation mechanism and was successfully shown recently using continuous wavelet transform by Li *et al.* [29–31]. The wavelet transform technique adds time resolution to the frequency, enabling us to see the temporal characteristics of the signals and their associated frequency. The continuous wavelet transform (CWT) [58] breaks down a given signal into a time-scale space and its squared magnitude. This technique overcomes the shortcomings of the Fourier analysis by adding the time resolution. The continuous wavelet transform (CWT) method employed in the current study is defined as,

$$W_x(a,\tau) = \int_{-\infty}^{+\infty} x(t)\,\psi^*_{a,\tau}(t)\,\mathrm{d}t, \tag{6}$$

where $W_x(a,\tau)$ is the continuous wavelet transform of function $x(t)$, $a > 0$ is the scale variable, τ is the time delay, $\psi_{a,\tau}(t)$ is the wavelet function, and the symbol $*$ denotes the complex conjugate. The continuous translation and dilation of the mother wavelet $\psi(t)$ are obtained by

$$\psi^*_{a,\tau}(t) = \frac{1}{\sqrt{a}}\,\psi^*\,(\frac{t-\tau}{a}). \tag{7}$$

The Morlet wavelet [59] was chosen as the wavelet function for the analysis, given by,

$$\psi(t) = \Pi^{-1/4} e^{iw_o t} e^{-(-t^2/2)}, \tag{8}$$

where w_0 is the non-dimensional frequency and is chosen to be 6.0 to satisfy the wavelet admissibility condition [60].

The contour plots of the wavelet coefficient magnitude for the pressure signal collected by the near-field pressure transducer M1 for the three tested configurations at the angle of attack $\alpha = 14°$ and $18°$ are presented in Fig. 23. Even though the measurements were carried out for 16 seconds, the results are presented only for 0.6 seconds with a higher temporal resolution for better visualisation. The frequency variation with time is evidently visible in the presented results for all the configurations. For the Baseline airfoil, the Rossiter modes are distinctly evident. In Fig. 23 (a) and (b), the high temporal resolution of the results clearly show that the modes are amplitudes modulated in time. However, only the first four modes are clearly seen with the mode two (St_2) possessing the highest level of energy. The results for the angle of attack $\alpha = 14°$ distinctly display this behaviour, whereas at the angle of attack $18°$ the results have higher amplitude with increased occurrences, making it harder to spot the mode amplitude modulation. The absence of the Rossetier modes for the H-SCF and SCF configuration are also clearly seen in the results shown in Fig. 23. The behaviour of the modes switching in time was previously shown by Kergerise *et al.* [61] for cavity flow and by Li *et al.* [30, 31] for a 30P30N high-lift airfoil. These studies showed that at a given time period the cavity resonates at a given mode or modes but the modes modulate and interact amongst themselves [30, 31, 61]. This is expected as the mode number of the cavity oscillation is related to the spacing between the vortices [61].

In order to further understand the multiple tone generation mechanism seen in the current study, power spectral density of the time signal and the wavelet coefficient magnitude ($\mid W_x^2 \mid$)

at selected frequencies St_{2-10} (see Table 4) are presented in Fig. 24. The results in Fig. 24 shows the amplitude of the wavelelet coefficient magnitude ($E(St_s)$) in terms of slat chord-based Stouhal number (St_s). The presented results show that that at the angle of attack $\alpha = 14°$, for modes 3 and 4, the amplitude is modulated by a frequency $\Delta St_{3,4} = 1.603$ and at the angle of attack 18°, for mode 5, 7 and 10, the amplitude is modulated by a frequency $\Delta St_{5,7,10} = 1.729$. The amplitude modulation frequency found for various Morlet scales (a), in Eq. 8, are the primary acoustic energy concentrated at mode 2, which is also referred to as St_2 (see Table 4). The modulation phenomenon states that the secondary frequencies can be predicted by the following [30, 31],

$$St_n = St_{n.max} \pm k \cdot \Delta St_s, \tag{9}$$

where k is the positive integer, $St_{n.max}$ is the frequency of the primary tone, ΔSt_s is the modulation frequency. By applying the calculated modulation frequency in Eq. 9, for the angle of attack $\alpha = 18°$, several secondary frequencies can be predicted as $St_5 = St_3 + \Delta St_s = 3.4$, $St_6 = St_4 + \Delta St_s = 2.215$ and $St_6 = St_4 + \Delta St_s = 4.3$, etc. This equation can also be used to predict all the weaker tones observed in Fig. 18. The results show that the relationship between the tonal peaks are not only confined to the amplitude modulation phenomenon but they also have a harmonic and a non-linear relationship between themselves as shown in Table 4 and will be further discussed in the following sections.

4.6. Higher order spectral analysis

The turbulent cascade phenomena of fluids can be well characterized by identifying the non-linear exchange of energy from one frequency to another. In order to identify and interpret the non-linear energy transfer between the frequencies, the higher order spectral analysis, namely auto-bispectrum was carried out. This method was successfully used to show the non-linear interactions between the Rossiter modes in cavity flows [61]. In a recent study, Pascioni and Cattafesta [27] showed the mode interaction phenomenon in slat cavity flow. It is well known that the phase information is suppressed by the power spectral density, making higher order spectral methods as an essential tool to quantify the quadratic phase coupling between frequencies as they retain the phase information. If several tonal peaks are present in the power spectral density the number of independent sources cannot be identified but auto-bicoherence allows one to discover if a tonal peak has been created by the quadratic nonlinear interaction. The auto-bispectrum (B_{ppp}) is used to determine the quadratic coupling and algebraic sum between the frequencies f_i and f_j and it is calculated from,

$$B_{ppp}(f_i, f_j) = \lim_{T\to\infty} \frac{1}{T} EV[P(f_i)P(f_j)P^*(f_i + f_j)], \tag{10}$$

where $P(f)$ is the Fourier Transform of $p(t)$, T is the time length, $EV[\cdot]$ is the expected value and $*$ denotes the complex conjugate. The auto-bispectrum can also be normalized by the corresponding power spectrum elements, known as the auto-bicoherence, as follows,

$$b^2_{ppp}(f_i, f_j) = \frac{\mid B_{ppp}(f_i, f_j) \mid^2}{\Phi_{pp}(f_i + f_j)\Phi_{pp}(f_i)\Phi_{pp}(f_j)}. \tag{11}$$

The auto-bicoherence between the three waves measures their phase coupling. If the frequencies of the wave at f_i, f_j and $f_i + f_j$ are characterised by statistically independent

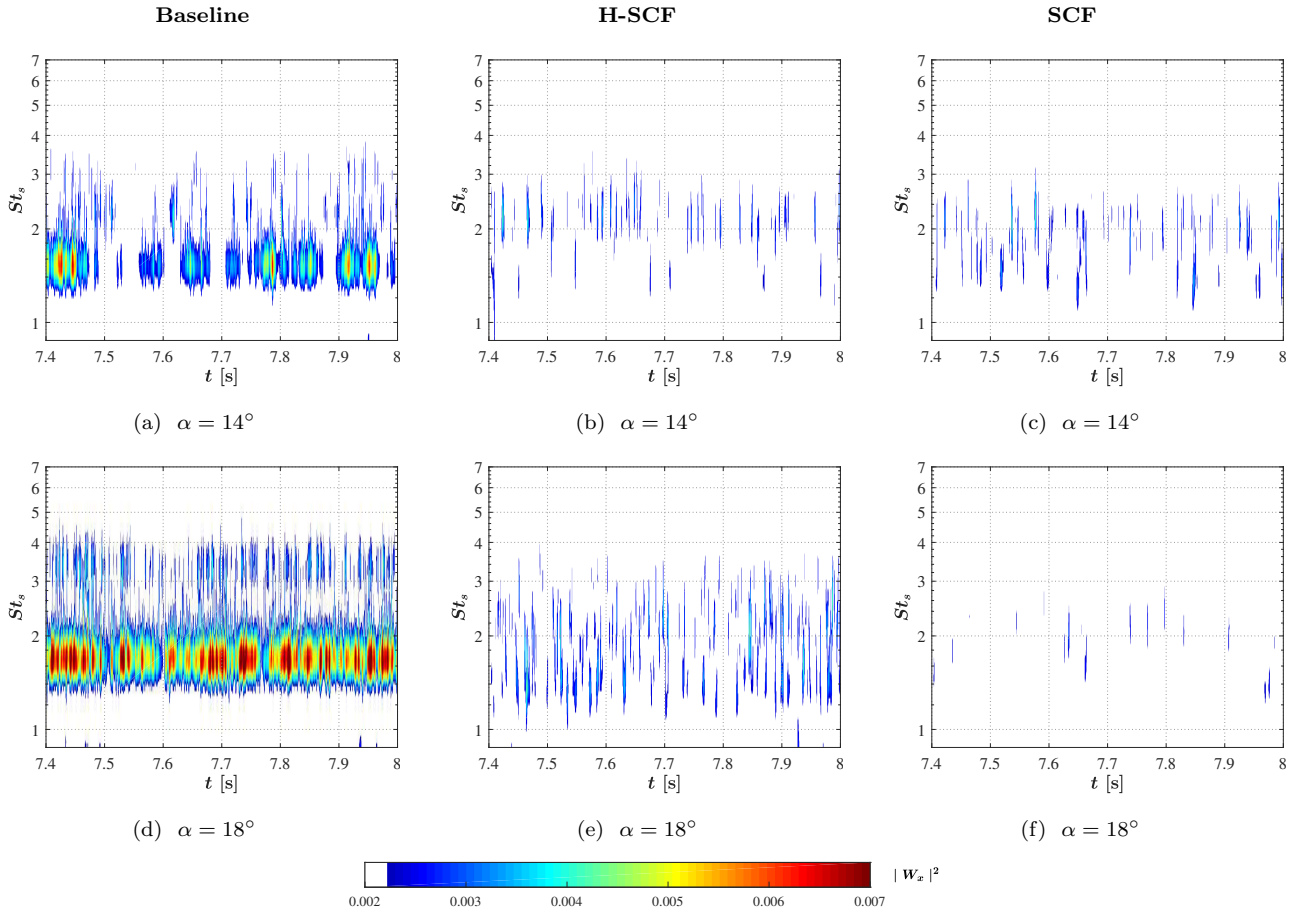

Figure 23: The contours of the wavelet coefficient magnitude ($|W_x^2|$) for the near-field pressure transducer M1 calculated using Morlet wavelet function.

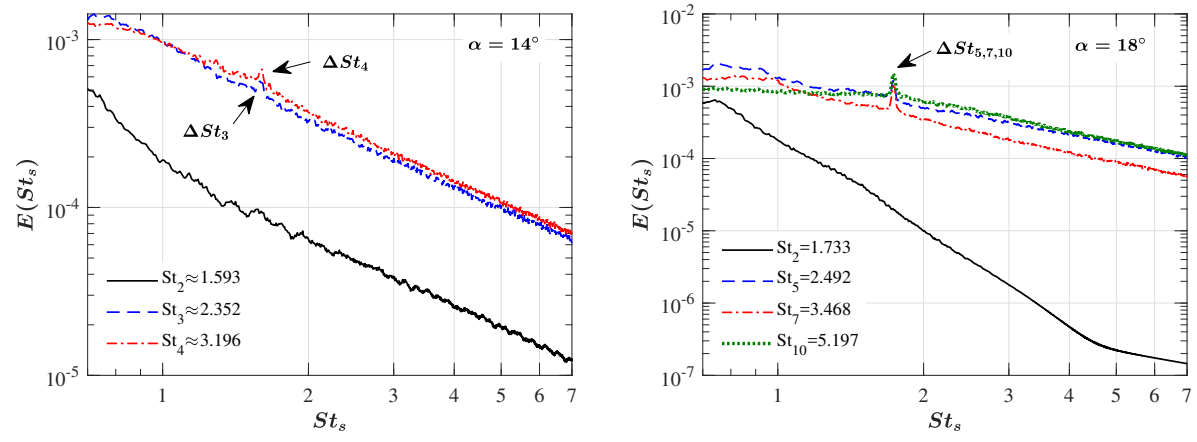

Figure 24: Power spectral density of time signal and wavelet coefficient at selected resonance frequencies (St_n) from Table 4.

phase relationship, then $b^2_{ppp} = 0$. If the frequency component at $f_i + f_j$ exhibits any phase relationship with f_i and f_j, then the corresponding auto-bicoherence will have a value, as $0 < b^2_{ppp} < 1$. If the waves are perfectly quadratically coupled, then $b^2_{ppp} = 1$.

The contour plots of the auto-bicoherence for the unsteady surface pressure transducer signal at M1 at the angle of attack $\alpha = 18°$ for all the three configurations are presented in Fig. 25. The sum of the frequencies is shown only up to the region of interest (St_{12}, St_{12}). For the Baseline case, in Fig. 25a, it is evident from the results that the multiple peaks have quadratic coupled modes. The slat cavity modes self interact $(St_1, St_1), (St_2, St_2), (St_3, St_3)$, etc. and also generate harmonics. The results clearly show that the even modes $(St_{2,4,...12})$ have a stronger bicoherence compared to the odd modes $(St_{1,3...11})$. As mentioned above, if a tonal peak is created by non-linear interaction, the bicoherence value would be $b^2_{ppp} = 1$. For the frequencies $St_{4\&6}$, the bicoherence value is $b^2_{ppp} > 0.85$, indicating that these harmonics $St_4 = 2St_2$ and $St_6 = 3St_2$ are possibly generated by quadratic coupling. Moreover, a large degree of phase coupling is seen for all the even modes. To further analyze, let us first consider only the odd modes. The results show that there is an interaction between (St_1, St_1) and a mild interaction between (St_1, St_3), but then no phase coupling for St_1 with any other mode. When considering the third mode St_3, it shows coupling only with St_4 and St_6. The only other odd mode to show phase coupling behavior is (St_5, St_6). Therefore, it is clear that the observed odd modes are not in phase with themselves but are occasionally phase coupled with St_4 and St_6. The even modes show a very large degree of phase coupling with most of the observed modes. For the mode St_2, results show phase coupling with all the other modes, including the odd modes, except for the St_3 and St_4 modes. All the other even modes $(St_{2,4...12})$ show phase coupling with all the other odd and even modes to some degree, but their degree of phase coupling with the even modes are much higher. The results show a high level of quadratic coupling with some of the modes and no coupling between some modes. This shows that the modes reinforce each other in a way at times or exist on their own in some instances. The strong self-interaction of the first mode St_1 with no cross interaction is suggestive that the first mode might be of a different source and nature.

The bicoherence results for the H-SCF and SCF configurations are presented in Figs. 25b and 25c. The results for the H-SCF and SCF configuration show self-interaction of the broadband hump $0.5 < St_s < 4$ observed in both the cases. This broadband hump was the most dominant feature seen in the near-field unsteady surface pressure results and spanwise coherence results in Fig. 18 and 19, respectively for the H-SCF and SCF configurations. Even though the bicoherence of the broadband hump is not higher than $b^2_{ppp} \approx 0.05$, they are still statistically significant due to a large number of averages used for the bicoherence calculations. The results show that the self-interaction occurs at St_2 for both the H-SCF and SCF configurations. The results here show strong self-interaction of the tones for the Baseline case. The use of the H-SCF and SCF configuration does not only eliminate the tone but also the constructive self-interaction that arise from it. The results are not presented for the angle of attack $\alpha = 14°$ as they showed insignificant self and cross coupling between the tones due to their weaker tones and weaker vortex shedding as seen in Figs. 18 and 21.

4.7. Persistence spectrum

The interference between two acoustic waves can be constructive or destructive depending on their phase difference. The phase coupling and interference of the signals can be visualized

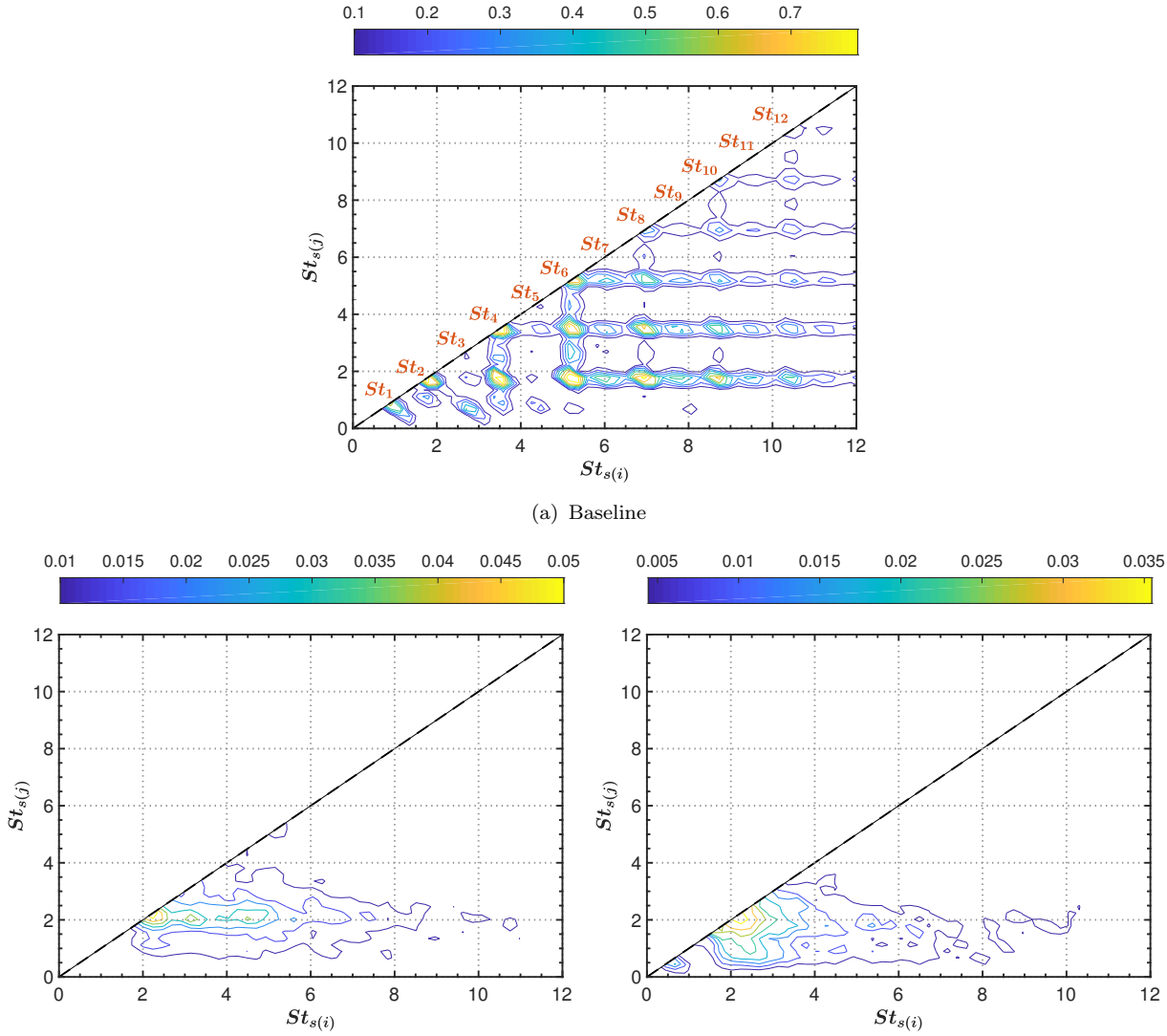

(a) Baseline

(b) H-SCF

(c) SCF

Figure 25: The auto-bicoherence contour for the transducer M1 on the main-element for the angle of attack $\alpha = 18°$ labelled with the associated modes (St_n) for the Baseline case detailed in Table 4.

using the persistence spectrum. To further understand the nature of the observed peaks in the present study, the unsteady surface transducer signals from the near-field pressure transducer M1 on the main-element is used to plot the persistence spectrum. The persistence spectrum is a histogram in power-frequency space that shows the percentage of the time that a given frequency is present in a given signal. The time percentage shown as density contours has a higher value in the results if a particular frequency persists in a signal for a longer period of time [62]. The persistence spectrum was calculated for the entire measured time signal of 16 seconds. The short-time Fourier transform for the persistence spectrum was carried out for a time resolution of 0.04 seconds and a frequency resolution of $St_s = 0.45$. The results for all the three tested configurations at the angle of attack $\alpha = 18°$ are presented in Fig. 26. The results for the Baseline configuration clearly show that the $St_2 = 1.733$ i.e., the vortex shedding frequency, holds the primary acoustic energy as it is present through the entire time

period. The harmonics of the second mode $St_{4,6,8}$ hold the next highest energy over the time period. All the odd modes, which do not have any phase relation (see Fig. 25) with the even modes clearly have lesser magnitude and their energy is distributed over time. These results for the Baseline are yet again suggestive that the odd modes might have a different source compared to the even modes. The results for the H-SCF and SCF configurations clearly show that their noise is of broadband nature and is spread over the entire time period. The spectral hump at St_1 is not dominated over time, rather the energy of the broadband spectra is evenly distributed in time over the entire frequency range.

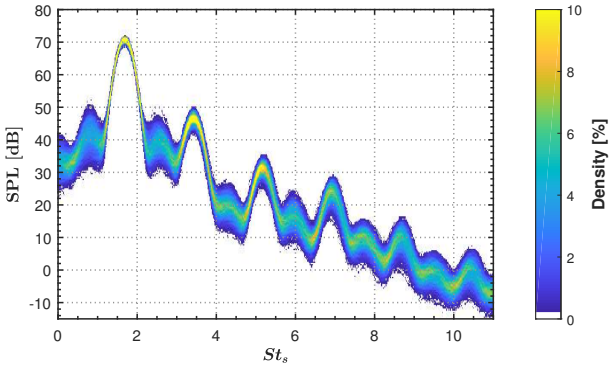

(a) Baseline

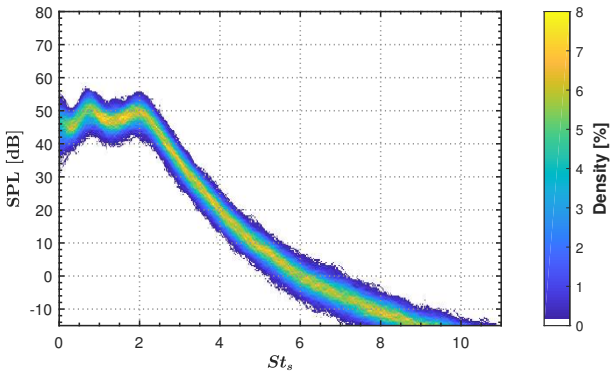

(b) H-SCF

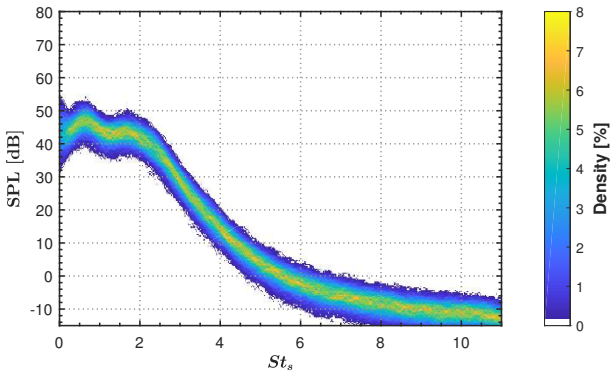

(c) SCF

Figure 26: The persistence spectrum contour for the near-field pressure transducer M1 on the main-element at angle of attack $\alpha = 18°$.

5. Conclusions

The aerodynamic and aeroacoustic characteristics of 30P30N airfoil with and without slat cove fillers were investigated. As part of the noise reduction study of the MDA 30P30N airfoil, a half slat cove filler (H-SCF) and a slat cove-filler (SCF) configuration along with a Baseline configuration were considered. Results have shown that the aerodynamic lift and drag measurements exhibit an insignificant difference between the tested configurations. The H-SCF had the best performance relative to the Baseline and all the SCF configuration in terms of the lift-to-drag ratio and the drag-polar plots. The coefficient of pressure distribution results show that the application of the slat cove fillers decreased the suction peak by up to 15% over the main-element of the airfoil. The near-field surface pressure measurements show increased noise at low-frequency for the H-SCF and SCF configurations, which is due to the non-propagating hydrodynamic of the flow field within the slat and main-element as this noise increase is not observed in the far-field measurements. The results also clearly show that the far-field noise measurements and the overall sound pressure level can be significantly reduced by up to $5 - 9$ dB with the application of the slat cove fillers. The lateral coherence studies have shown that a high level of coherence is present for all the configurations, particularly with a distinct broadband spectral humps at low-frequency for cases with the slat cove fillers. The contour plots of the wavelet coefficient show that the Rossiter modes for the Baseline case are amplitudes modulated in time, however, these modes are absent for the configuration with slat cove fillers. The results of the higher spectral order analysis show that the Rossiter modes that arise from the slat cavity of the Baseline case display quadratic interaction amongst themselves. The experimental work in this paper shows that there is a need for more fundamental research on the low-frequency broadband hump ($St_s = 0.5 - 1$) that arises in the high-lift device slat noise. This paper also shows that the application of the slat cove fillers eliminate the modes generated by the slat cavity and reduces broadband noise without compromising the aerodynamic performance of the high-lift device.

Acknowledgment

The authors would like to acknowledge the financial support provided by Embraer.

[1] Kamliya Jawahar, H., Azarpeyvand, M., and Carlos R.Ilario. "Aerodynamic and Aeroacoustic Performance of Three-element High Lift Airfoil fitted with Various Cove Fillers", AIAA 2018-3142, 2018.

[2] Kamliya Jawahar, H., Azarpeyvand, M., and Carlos R.Ilario. "Experimental Investigation of Flow Around Three-Element High-lift Airfoil with Morphing Fillers", AIAA 2017-3364, 2017.

[3] Ai, Q., Kamliya Jawahar, H., and Azarpeyvand, M., "Experimental Investigation of Aerodynamic Performance of Airfoils Fitted with Morphing Trailing Edges", AIAA 2016-1563, 2016.

[4] Kamliya Jawahar, H., Ai, Q., and Azarpeyvand, M., "Experimental and Numerical Investigation of Aerodynamic Performance of Airfoils Fitted with Morphing Trailing Edges", AIAA 2017-3371, 2017.

[5] Kamliya Jawahar, H., Ai, Q., and Azarpeyvand, M., "Experimental and Numerical Investigation of Aerodynamic Performance of Airfoils with Morphed Trailing Edges", *Renewable Energy*, Vol. 127, 2018, pp. 355-367.

[6] Liu, H.R., Azarpeyvand, M., Wei, J.J., and Qu, Z.G., "Tandem Cylinder Aerodynamic Sound Control Using Porous Coating", *Journal of Sound and Vibration*, Vol. 334, 2015, pp. 190-201.

[7] Showkat Ali, S. A., Azarpeyvand, M., and Ilario, C., "Trailing Edge Flow and Noise Control using Porous Treatments", *Journal of Fluid Mechanics*, Vol. 850, 2018, pp. 83-119.

[8] Showkat Ali, S. A., Szoke, M., Azarpeyvand, M., and Ilario, C., "Turbulent Flow Interaction with Porous Surfaces", AIAA 2018-2801, 2018.

[9] Afshari, A., Azarpeyvand, M., Dehghan, A. A., and Szoke, M., "Trailing Edge Noise Reduction Using Novel Surface Treatments", AIAA 2016-2834, 2016.

[10] Liu, X., Kamliya Jawahar, H., Azarpeyvand, M., and Theunissen, R. "Aerodynamic Performance and Wake Development of Airfoils with Serrated Trailing Edges", *AIAA Journal*, Vol. 55, No. 11, 2017, pp. 3669-3680.

[11] Lyu, B., Azarpeyvand, M., and Sinayoko, S., "Prediction of Noise from Serrated Trailing Edges", *Journal of Fluid Mechanics*, Vol. 793, 2016, pp. 556-588.

[12] Khorrami, M., Berkman, M. and Choudhari, M., "Unsteady Flow Computations of a Slat with a Blunt Trailing Edge", *AIAA Journal*, Vol. 38, No. 11, 2000, pp. 2050-2058.

[13] Roger, M., and Perennes, S., "Low-Frequency Noise Source in Two Dimensional High-lift Devices", AIAA 2000-1972, 2000.

[14] Olson, S., Thomas, F., and Nelson, R., "Mechanisms of Slat Noise Production in a 2D Multi-element Airfoil Configuration", AIAA 2001-2156, 2001.

[15] Khorrami, M., "Understanding Slat Noise Sources", Colloquium EUROMECH, Vol. 449, 2003.

[16] Choudhari, M., and Khorrami, M., "Effect of Three-dimensional Shear-layer Structures on Slat Cove Unsteadiness", *AIAA Journal*, Vol. 45, No. 9, 2007, pp. 21742186.

[17] Kolb, A., Faulhaber, P., Drobietz, R., and Grunewald, M., "Aeroacoustic Wind Turbine Measurements on a 2D High-lift Configuration", AIAA 2007-3447, 2007.

[18] Mendoza, J. M., Brooks, T. F., and Humphreys, W. M., "An Aeroacoustic Study of a Leading Edge Slat Configuration", *International Journal of Aeroacoustics*, Vol. 1, No. 3, 2002, pp. 241-274.

[19] Hein, S., Hohage, T., Koch, W., and Schoberl, J., "Acoustic Resonances in a High-lift Configuration", *Journal of Fluid Mechanics*, Vol. 582, 2007, pp. 179-202.

[20] Makiya, S., Inasawa, A., and Asai, M., "Vortex Shedding and Noise Radiation from a Slat Trailing Edge", *AIAA Journal*, Vol. 48, No. 2, 2010, pp. 502-508.

[21] Murayama, M., Nakakita, K., Yamamoto, K., Ura, H., Ito, Y., and Choudhari, M., "Experimental Study of Slat Noise from 30P30N Three-element High-lift Airfoil in JAXA Hard-wall Low-speed Wind Tunnel", AIAA 2014-2080, 2014.

[22] Terracol, M., Manoha, E., and Lemoine, B., "Investigation of the Unsteady Flow and Noise Generation in a Slat Cove", *AIAA Journal*, Vol. 54, No. 2, 2016, pp. 469-489.

[23] Choudhari, M., and Lockard D. P., "Assessment of Slat Noise Predictions for 30P30N HighLift Configuration from BANC-III Workshop", AIAA 2015-2844 , 2015.

[24] Pagani, C. C., Souza, D. S., and Medeiros, M. F., "Slat Noise: Aeroacoustic Beamforming in Closed-section Wind Tunnel with Numerical Comparison", *AIAA Journal*, Vol. 54, No. 7, 2016, pp. 2100-2115.

[25] Pagani, C. C., Souza, D. S., and Medeiros, M. F., "Experimental Investigation on the Effect of Slat Geometrical Configuration on Aerodynamic Noise", *Journal of Sound and Vibration*, Vol. 394, 2017, pp. 256-279.

[26] Pascioni, K. A., and Cattafesta, L. N., "An Aeroacoustic Study of a Leading-edge Slat: Beamforming and Far-field Estimation using Near-field Quantities", *Journal of Sound and Vibration*, Vol. 429, 2018, pp. 224-244.

[27] Pascioni, K. A., and Cattafesta, L. N., "Unsteady Characteristics of a Slat-cove Flowfield", *Physical Review Fluids*, Vol. 3, 2018, pp. 1-27.

[28] Li, L., Liu, P., Guo, H., Hou, Y., Geng, X., and Wang, J., "Aeroacoustic Measurement of 30P30N High-lift Configuration in the Test Section with Kevlar Cloth and Perforated Plate", *Aerospace Science and Technology*, Vol. 70, 2017, pp. 590-599.

[29] Li, L., Liu, P., Guo, H., Geng, X., Hou, Y., and Wang, J., "Aerodynamic and Aeroacoustic Experimental Investigation of 30P30N High-lift Configuration", *Applied Acoustics*, Vol. 132, 2018, pp. 43-48.

[30] Li, L., Liu, P., Xing, Y., and Guo, H., "Time-frequency Analysis of Acoustic Signals from a High-lift Configuration with two Wavelet Functions", *Applied Acoustics*, Vol. 129, 2018, pp. 155-160.

[31] Li, L., Liu, P., Xing, Y., and Guo, H., "Wavelet Analysis of the Far-field Sound Pressure Signals Generated from a High-lift Configuration", *AIAA Journal*, Vol. 56, No.1, 2018, pp. 432-437.

[32] Horne, W. C., James, K. D., Arledge, T. K., Soderman, P. T., Field, M., Burnside, N., and Jaeger, S. M., "Measurement of 26%-scale 777 Airframe Noise in the NASA Ames 40-by-80 foot Wind Tunnel", AIAA 2005-2810, 2005.

[33] Streett, C., Casper, J., Lockard, D., Khorrami, M., Stoker, R., Elkoby, R., Wenneman, W., and Underbrink, J., "Aerodynamic Noise Reduction for High-lift Devices on a Swept Wing Model", AIAA 2006-212, 2006.

[34] Andreou, C., Graham, W., and Shin, H. C., "Aeroacoustic Study of Airfoil Leading Edge High-lift Devices", AIAA 2006-2515, 2006.

[35] Andreou, C., Graham, W., and Shin, H. C., "Aeroacoustic Comparison of Airfoil Leading Edge High-lift Geometries and Supports", AIAA 2007-230, 2007.

[36] Imamura, T., Ura, H., Yokokawa, Y., Enomoto, S., Yamamoto, K., Hirai, T., Group, A. P., and Division, E. S., "Designing of Slat Cove Filler as a Noise Reduction Device for Leading-edge Slat", AIAA 2007-3473, 2007.

[37] Ura, H., Yokokawa, Y., Imamura, T., Ito, T., and Yamamoto, K., "Investigation of Airframe Noise from High Lift Configuration Model", AIAA 2008-19, 2008.

[38] Shmilovich, A., Yadlin, Y., and Pitera, D. M., "Wing Leading-edge Concepts for Noise Reduction", 27th International Congress of the Aeronautical Sciences, ICAS 2010-5.2.2, 2010.

[39] Shmilovich, A., Yadlin, Y., and Company, T. B., "High-lift Systems for Enhanced Take-off Performance", 28th International Congress of the Aeronautical Sciences, 2012, pp. 1-13.

[40] Scholten, W. D., Hartl, D. J., Turner, T. L., and Kidd, R. T., "Development and Analysis-Driven Optimization of Superelastic Slat-cove Fillers for Airframe Noise Reduction", *AIAA Journal*, Vol. 54, No. 3, 2016, pp. 1078-1094.

[41] Tao, J., and Sun, G., "A Novel Optimization Method for Maintaining Aerodynamic Performances in Noise Reduction Design", Aerospace Science and Technology, Vol. 43, 2015, pp. 415-422.

[42] Zhang, Y., Neill, A., and Cattafesta, L. N., "Assessment of Noise Reduction Concepts for Leading-Edge Slat Noise", AIAA 2018-3461, 2018.

[43] Mayer, Y., Kamliya Jawahar, H., Szoke, M., and Azarpeyvand, M., "Design of an Aeroacoustic Wind Tunnel Facility at the University of Bristol", AIAA 2018-3138, 2018.

[44] Mayer, Y., Kamliya Jawahar, H., Szoke, M., Ali, S. A. S., and Azarpeyvand, M., "Design and Performance of an Aeroacoustic Wind Tunnel Facility at the University of Bristol", Applied Acoustics, Vol. 155, 2019, pp. 358-370.

[45] Pascioni, K. A., "An Aeroacoustic Characterization of a Multi-Element High-Lift Airfoil", PhD Thesis, Florida State University, 2017.

[46] Manoha, E., and Pott-Polenske, M., "LEISA2: An Experimental Database for the Validation of Numerical Predictions of Slat Unsteady Flow and Noise", AIAA 2015-3137, 2015.

[47] Garcia-Sagrado, A., and Hynes, T., "Wall-Pressure Sources Near an Airfoil Trailing Edge Under Separated Laminar Boundary Layers", *AIAA Journal*, Vol. 49, No. 9, 2011, pp. 1841-1856.

[48] Garcia-Sagrado, A., and Hynes, T., "Stochastic Estimation of Flow Near the Trailing Edge of a NACA 0012 Airfoil", *Experiments in Fluids*, Vol. 51, No. 4, 2011, pp. 1057-1071.

[49] Garcia-Sagrado, A. and Hynes, T., "Wall Pressure Sources Near an Airfoil Trailing Edge under Turbulent Boundary Layers", *Journal of Fluids and Structures*, Vol. 30, 2012, pp. 3-34.

[50] Showkat Ali, S. A., Azarpeyvand, M., Szoke, M. and Ilario, C., "Boundary layer flow interaction with a permeable wall", Physics of Fluids 30, 085111, 2018.

[51] Valarezo, W. O., "High-Lift Testing at High Reynolds Numbers", AIAA 92-3986, 1992.

[52] Valarezo, W. O., Dominik, C. J., and Mcghee, R. J., "Reynolds and Mach Number Effects on Multi-element Airfoils", N93-27446, 1992.

[53] Chin, V. D., Peters, D. W., Spaid, F. W., and Mc Ghee, R. J., "Flow-field Measurements About a Multi-element Airfoil At High Reynolds Numbers", AIAA 93-3137, 1993.

[54] Olson, S., Thomas, F., and Nelson, R., "A Preliminary Investigation into Slat Noise Production Mechanisms in a High-lift Configuration", AIAA 2000-4508, 2000.

[55] Takeda, K., Asdcroft, G.B., and Zhang, X., "Unsteady Aerodynamics of Slat Cove Flow in a High-lift Device Configuration", AIAA 2001-0706, 2001.

[56] Rossiter, J., "Wind Tunnel Experiments on the Flow Over Rectangular Cavities at Subsonic and Transonic Speeds", Royal Aircraft Establishment ARC R&M 3238, 1966.

[57] Heller, H. H, and Bliss, D. B, "The Physical Mechanism of Flow-induced Pressure Fluctuations in Cavities and Concepts for their Suppression", AIAA 1975-491, 1975.

[58] Mallat, S., "A Wavelet Tour of Signal Processing", Elsevier, 1999.

[59] Morlet, J., "Sampling Theory and Wave Propagation", Proceedings of the 51st Annual Meeting of the Society Exploration Geophysics, 1981.

[60] Farge, M., "Wavelet Transforms and their Application to Turbulence", *Annual Review of Fluid Mechanics*, Vol. 24, 1992, pp. 395-457.

[61] Kegerise, M., Spina, E., Garg, S., and Cattafesta, L., "Mode-switching and Non-linear Effects in Compressible Flow over a Cavity", *Physics of Fluids*, Vol. 16, pp. 678-687, 2004.

[62] MathWorks, "Signal Processing Toolbox: R2018b Documentation", 2018.

[63] Auger, F., Flandrin P., Gonalvs P., Lemoine, O., "Time-Frequency Toolbox". CNRS France-Rice University, 1996.

[64] Swami, A., Mendel J. M., Nikias C. L., "Higher-order Spectral Analysis Toolbox" The Mathworks Inc, 1998.